J. Plasma Physics (2008), *vol.* 74, *part* 3, *pp.* 391–429. © 2007 Cambridge University Press
doi:10.1017/S0022377807006927 Printed in the United Kingdom

High-enthalpy, water-cooled and thin-walled ICP sources: characterization and MHD optimization

G. HERDRICH[1,2] and D. PETKOW[1]

[1]Institut für Raumfahrtsysteme (IRS), Universität Stuttgart,
Pfaffenwaldring 31, 70569 Stuttgart, Germany
(herdrich@irs.uni-stuttgart.de)

[2]Steinbeis Transferzentrum Plasma- and Space Technology,
c/o Institut für Raumfahrtsysteme (IRS), Universität Stuttgart,
Pfaffenwaldring 31, 70569 Stuttgart, Germany
(info@plasma-raumfahrt.de)

(Received 15 May 2007 and in revised form 16 October 2007, first published online 6 December 2007)

Abstract. The development of the inductively driven plasma wind tunnel PWK3, which enables the electrodeless generation of high-enthalpy plasmas for the development of heat shield materials required for space vehicles performing entry manoeuvres in the atmospheres of Venus, Earth and Mars, is described. The facility with its modular inductive plasma generators allows operation with gases such as carbon dioxide, air, oxygen and nitrogen and was qualified for thermal plasma powers up to 60 kW. Previously developed models for determining plasma properties and plasma source related characteristics enable a maximum plasma power in combination with long operational periods using different operational gases and gas mixtures. This is achieved by an optimization using the optimum operational frequency, a minimization of field losses using very thin plasma tube wall thicknesses and the successful application of MHD effects. Based on the solved cylinder problem for ICPs, a one-dimensional model for radial Lorentz forces and magnetic pressure has been developed. Here, a synthesis of previously published data and works is made where the new algebraic model for the calculation of Lorentz forces and magnetic pressures in an ICP was used and applied to experimental data. In addition, results from the model using the experimental data are shown to be consistent and, in addition, a comparison with a simpler model based on the well-known exponential approach for ICPs showed that the simpler model is covered without fail by the new model. The new model also states that there is a maximum of the Lorentz forces over the damping parameter d/δ (plasma diameter divided by skin depth) which almost corresponds with the position of the maximum plasma power of the cylindric model for ICPs. For the magnetic pressure the position of the maximum pressure is identical to the value for d/δ for the maximum plasma power.

1. Introduction

The inductive discharge in a cylindrical container has been the topic of scientific investigations for the past 100 years and used for just as long. In 1884 Hittorf,

https://doi.org/10.1017/S0022377807006927 Published online by Cambridge University Press

who invented inductively heated plasma systems, described the first devices based on power induction into a plasma [1]. Fundamental experiments on the physics of plasmas were often performed where low electric power, as was available in the systems used in the first 75 years after Hittorf, was sufficient. So near the end of the 19th century, Hittorf investigated the discharge behavior of various gases at low densities.

The discharge in a cylindrical container, which is surrounded by a cylindrical coil, is either caused by the axial electric field E_z or by the circumferential field E_ϕ and is maintained by the oscillating axial magnetic field [2]. However, there are then fundamental differences between the accompanying discharges. The intensity profiles measured with the ICP source IPG3 (inductively heated plasma generator) [3] in the context of the characterization of PWK3 characterize this type of discharge. While at low power levels a weakly lit discharge occurs, which is essentially an intensity maximum in the middle of the container, when the power is increased a discrete transition to a ring discharge near the surface of the container's inner wall of the plasma generator occurs. This observation conforms with MacKinnon's description. The first discharge condition can be described as an effect of the axial electric field between the coil ends, whereby inductive power is being dealt with by ring discharges. The inductive mode occurs when the flows into the induction coil are large enough to induce a circumferential electric field which can keep the ionization process going. As this mode is caused by the axial field and occurs at low power levels, to generate high-enthalpy plasma flows during entry simulation only the inductive mode is important. However, the transition between the two modes described here is highly dependent on the operational parameters, such as pressure, type of gas and operational frequency, so that knowledge of the influential parameters for generating high-enthalpy flows is important.

Pure induction of energy into a plasma was first described by Thomson using a transformer model [4]. Based on this, parameters such as plasma flow as well as the discharge voltage can be given dependent on the external electric parameters [5]. In addition, statements can be made about the qualitative behavior of external parameters dependent on the load, which is represented by the plasma. For several parameters, such as the plasma flow parameter, equations result which represent asymptotic approximations of detailed models. According to [6]

$$I_{\mathrm{Pl}} = nI_{\mathrm{coil}} \tag{1}$$

becomes

$$I_{\mathrm{Pl}} = n(I_{\mathrm{coil}} - I_{\mathrm{min}}) < nI_{\mathrm{coil}}. \tag{2}$$

Here n is the number of coil turns, I_{coil} is the coil current, I_{Pl} is the plasma flow and I_{min} the lowest possible power level necessary to maintain the inductive discharge. The deviance from the transformer (1) described in (2) is justified by the diamagnetism of the plasma, which occurs because of the field damping inside the plasma. The occurring plasma current is opposite to the coil current at all times. The result is that the plasma current establishes a magnetic field opposite to the coil's field. Both fields overlap and the magnetic field is reduced in a radial direction from the outside to the inside. The electric field which accompanies the time change in the axial magnetic field also decreases from the outside to the inside. A thin layer forms in which the main portion of the induction discharge occurs (skin effect).

https://doi.org/10.1017/S0022377807006927 Published online by Cambridge University Press

Thomson [7] presented mathematical models based on a uniform electric conductibility (σ_{eff}) of the volume considered here. The channel model of Freeman and Chase [8] is certainly comparable to Thomson's model. The expansion consists of the definition of two concentric zones whereby the outer ring is not electrically conductive. The interior cylinder, on the other hand, leads the entire plasma flow, whereby the electric conductibility is constant.

In the case of most of the authors mentioned thus far, collision processes in the discharge were not taken into account. This was taken into consideration by Eckert [9]. Henrikson et al. found a unified solution to the electrodynamic differential equations under the assumption of a parabolic distribution of the electric conductibility [10]. However, by considering such a profile, the variation of the ring discharge geometry becomes evident (e.g. the location of the maximum temperature). Additional parameters, such as the collision frequency, must then be varied in order to make comparisons with other measurements. This results in such a great multitude of possibilities out of all proportion in comparison to the remaining uncertainties and further assumptions (e.g. flow not being considered).

A model under the assumption of a constant effective σ_{eff} is presented here [11]. The focus was on relating the measurement data to the simple electrodynamic model. Furthermore, in the context of the measurements, comparisons with the model showed hints of electromagnetically induced flows. This could be confirmed by the unified solution of the radially directed Lorentz forces in the model. With an approach which uses the thermal power density in the model as a source term for one-dimensional heat conduction, a partially empirical equation to describe the radial intensity course in the plasma tube can be established.

Additional expansions to the models cannot be analytically solved *en masse* and lead to the use of iterative numerical methods. Boulos et al. were aware of the significance of the Lorentz forces based on their numerical calculations, which take the flow into consideration [12]. Miller and Ayen were among the first to numerically simulate inductively heated plasma sources [13]. These simulations resulted in radial temperature profiles of the plasma sources. Eckert [14] also analyzed the radial heat losses in 1969 using iterative methods. These calculations followed comparative numerical calculations from Pridmore-Brown [15]. Other authors expanded on Miller and Ayen's model. The motivation here was the consideration of a variety of gas flows, which was necessary for spectrochemical analyses based on feeding in various substances [16].

It should be pointed out that in the work discussed so far the systems investigated have a lower electrical power level than the inductive facilities used for entry simulation. The initial wattage is one or two orders of magnitude smaller than that in facilities used to generate high-enthalpy plasma flows where the plasma wattage reaches levels of at least 10^3 W. This has historical reasons because such high-performance systems were not built until the 1960s. Therefore, the uses of inductively heated plasma systems first belonged to spectral chemistry, which explains why most of the older work in this field can be found in this area. More extensive investigations of thermal RF plasmas occurred in the late 1970s and the 1980s. As early as 1980 Boulos et al. numerically examined the importance of gas injection. Here the authors could show that MHD flows could be used to lower the heat flux to the plasma container. The results of these tests confirm the experimental results and conclusions in [11] and in this paper. Later the group expanded their analyses with parameter investigations whereby they improved earlier models [17].

https://doi.org/10.1017/S0022377807006927 Published online by Cambridge University Press

In their observations McKelliget and El-Kaddah confirmed the significance of the Lorentz forces, whereby the reaction kinetics were observed more closely [18]. Improvements to the models and the computer systems made it possible to take the end effects of the coils into consideration, which are of particular importance at high frequencies [19].

The first high-performance facilities for atmospheric entry simulation in Russia [20] made it necessary to not just calculate the simulation of the plasma sources but also the high-enthalpy flows in the plasma wind tunnels [21] in order to describe the conditions in the plasma wind tunnel, especially the local quantities in the plasma stream and the interaction between the plasma and the thermal protection material. Non-equilibrium effects which are of significance for the plasma–wall interaction make the coupled calculation even more complex.

In the 1990s the first ICP-operated plasma wind tunnel facilities were conceived at IRS. After that facilities at the von Karman Institute (VKI) and at CORIA followed. Noteworthy work on numerical simulation has chiefly been carried out at VKI [22] and at IRS [23]. The VKI models are based on preliminary work by Mekidéche, who modeled inductively heated plasma generators on the basis of plasma generator technology with slotted copper coolers [24]. This technology is used at TSAGI to generate high-enthalpy flows with large cross sections. The VKI facility also uses a copper cooler inside the plasma vessel. At IRS this design was not pursued because the copper structure causes erosion by-products to result inside the discharge tube. This eliminates the significant advantage of inductively heated plasma generators, namely generating pure plasmas for catalytic investigations, for example.

At IRS, the advantage of electrode-less plasma generation accompanied by high plasma enthalpies is used, amongst others, for extensive (re-)entry experiments. The IPG design enables the generation of realistic entry plasma conditions regarding purity and variety of the plasma since carbonaceous, dusty or oxygen-containing working gases have a destructive influence on electrode-based plasma generators. Hence, numerous investigations concerning Mars, Venus and Titan's atmospheres have been performed at IRS [25].

In addition, basic investigations of thermal protection systems (TPSs) for (re-)entry bodies have been performed [26] leading to a fundamental understanding of complex surface processes such as catalysis [27], oxidation and active–passive transition [28]. As part of these investigations, appropriate plasma measurement techniques [29, 30] were developed. Moreover, flight qualification of sensor systems [31] has been performed and technical applications [32] have been developed using the IRS's IPG design and working principle. According to the different areas, three different plasma generators IPG3, IPG4 and IPG5 have been developed [5].

2. Set-up of PWK3

The PWK3 set-up shown in Fig. 1 consists of the IPG plasma source and the vacuum chamber [3, 5, 11]. The chamber is about 2 m in length and 1.6 m in diameter. Optical accesses enable the investigation of the plasma. A heat exchanger between the chamber and the vacuum system cools down the hot plasma to protect the vacuum system from being damaged. The flat lid of PWK3 (left side chamber) is equipped with the IPG and the external resonant circuit consisting of the capacitors with the connection to the IPG coil. The right side flange of the vacuum chamber is

https://doi.org/10.1017/S0022377807006927 Published online by Cambridge University Press

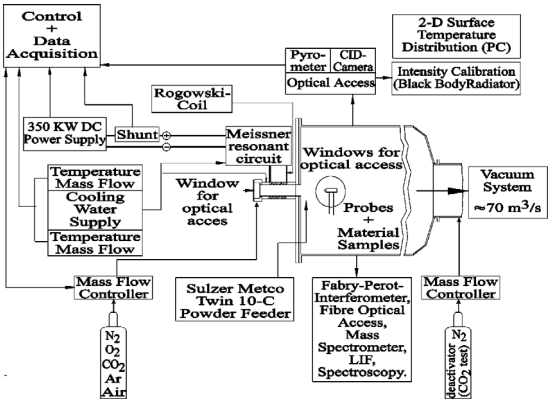


Figure 1. PWK3 facility set-up.

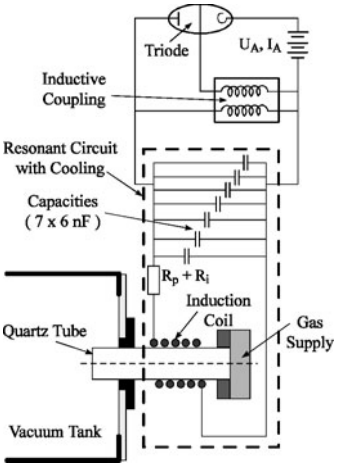


Figure 2. Scheme of the PWK3 Meissner-type resonant circuit.

connected to the IRS vacuum pump system simulating pressures at altitudes up to 90 km (Earth entry). Total suction power of the pumps amounts to 6×10^3 m^3 h^{-1} at atmospheric pressure and reaches about 2.5×10^5 m^3 h^{-1} at 10 Pa measured at the intake pipe of the system, which has a diameter of 1 m. The base pressure is about 0.5 Pa. The desired tank pressure can be adjusted between the best achievable vacuum and 100 kPa by removing one or more pumps from the circuit and/or mixing additional air into the system close to the pumps.

The external resonant circuit is water cooled. With this, the capacitors, which have a capacity of 6 nF $\pm$ 20% each, and the coil are cooled. The resonant circuit depicted in Fig. 2 is built in Meissner-type switching using a metal–ceramic triode with an oscillator efficiency of about 75%. Its nominal frequency can be changed by switching the number of capacitors k as well as by the use of coils with different inductivities (variation of coil turns, n).

For the investigations, a water-cooled 2.5-turn ($n = 2.5$) and 5.5-turn ($n = 5.5$) coil, each having a length l of 120 mm, were used. These configurations lead to inductivities L of 0.45 and 1.8 µH, respectively. The whole circuit is connected to

https://doi.org/10.1017/S0022377807006927 Published online by Cambridge University Press

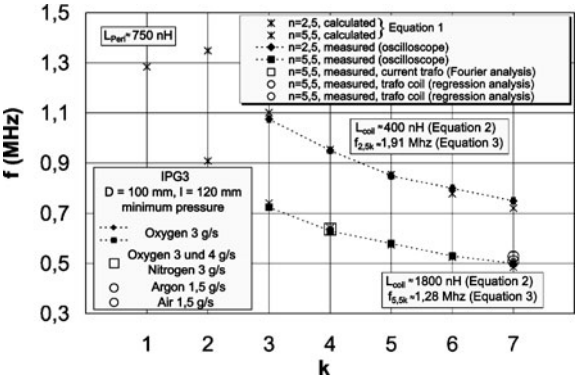


Figure 3. Measured operational frequencies ($n = 2.5, 5.5$) depending on number of capacitors.

a 375 kW power supply. The incoming anode power can be adjusted by controlling the anode (plate) voltage. Correspondingly, the frequency can be approximated by

$$\omega = 2\pi f \approx \frac{1}{\sqrt{LC}}. \tag{3}$$

Here, ω is the angular frequency while f is the frequency. The coil inductivity is calculated with

$$L_{\text{coil}} = d\alpha\left(\frac{d}{l}\right)n^2 \times 10^{-7} = g(d,l)n^2, \tag{4}$$

as the well-known relationship for long coils is no longer applicable [5]. The coil's diameter d has to be inserted in centimeters leading to the dimension Henry for L. The parameter α, a correction factor, has a magnitude of six. Introducing the parameter k for the number of capacitors used during operation, the frequency can be determined with

$$f_{n;k} = f(n,k) = f_{1;1}\frac{1}{n\sqrt{k}} \propto \frac{1}{n\sqrt{k}}. \tag{5}$$

Usually, there are peripherical inductivities owing to the coil's input leads which are not negligible. Therefore, it is useful to use (5) in empirical form depending on k, i.e. for coils with specific n.

With the coils used in this investigation ($n = 2.5, 5.5$), (3) and (4) deliver frequencies that are higher than the measured frequencies. This can be explained by the presence of peripherical inductivities which can be of the same order of magnitude as the coil inductivities:

$$L_{\text{tot}} = L_{\text{coil}} + L_{\text{Peri}}. \tag{6}$$

Equations (4)–(6) in combination with the measured frequencies for $n = 2.5$ and 5.5 lead to the frequency range shown in Fig. 3 for PWK3 using the inductively heated plasma generators IPG3, IPG4 and IPG5.

Figure 3 shows the measured frequencies of the facility PWK3 together with the calculated frequencies using (3) for different plasmas. Here, (6) was applied and L_{Peri} was calculated for all measured values. These values depend on the number of capacitors k and on the number of coil turns n. According to Fig. 3, this leads to a frequency range between 0.5 and 1.4 MHz. The usage of just one capacitor together

https://doi.org/10.1017/S0022377807006927 Published online by Cambridge University Press

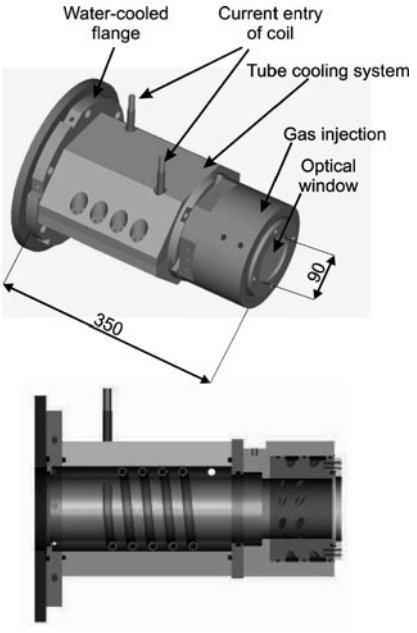


Figure 4. Inductively heated plasma source IPG3: assembly (top) and sectional drawing (bottom).

with a 2.5-turn coil ($L_{\mathrm{coil}} \approx 0.4$ µH) makes a frequency of 1.9 MHz achievable. This value cannot be operated permanently owing to the limitations of the energy supply system and current limiting effects that are ongoing with the capacity reduction. The second coil's ($n = 5.5$) inductivity is $L_{\mathrm{coil}} \approx 1.8$ µH. The frequencies shown with filled symbols were measured using a looped conductor connected to an oscilloscope. The open square symbol represents frequencies measured with a modified Pearson current monitor described in [5].

Here, the coil currents for $k = 4$ were measured with high time resolution for oxygen and nitrogen while varying the mass flow rate and anode power such that frequency spectra could be obtained by Fourrier analysis. For $k = 7$ a Rogowski coil was used to determine the frequencies for argon and air while varying the plate power. Regression analysis was performed for the data in [5]. With $L_{\mathrm{Peri}} \approx 0.75$ µH, (3)–(6) correspond well with the measured frequencies.

Inductively heated plasma generators basically consist of a coil surrounding a plasma container (tube) and capacitors. The alternating current in the coil induces a mostly azimuthal electric field inside the tube. This electric field initiates an electric discharge in the gas that is injected on one side into the tube (see Fig. 4). The produced plasma is expanded into the vacuum chamber. The plasma current amplitude, and thus the Ohmic heating, strongly depend on the electric conductivity of the plasma and the resonant frequency.

The principal parts of the plasma generators IPG3 and IPG4 are described here. An axial optical access through the inner injection head enables investigations of the plasma inside the generator. The tube cooling system is transparent. Hence, the position of the 'plasma flame' within the tube can be observed with regard to different operating parameters such as chamber pressure, working gas, mass

https://doi.org/10.1017/S0022377807006927 Published online by Cambridge University Press

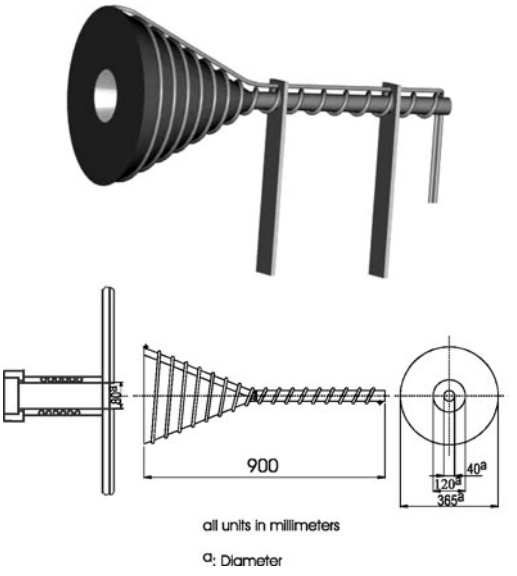


Figure 5. Calorimeter: three-dimensional drawing (top) and scheme in PWK3 with dimensions (bottom).

flow and anode power. In addition, this feature is supported by the axial optical window. The total length of IPG3 is about 0.35 m, its diameter about 0.1 m. The quartz tube contains the generated plasma which leaves the generator through the chamber adapter. The induction coil is connected to the external resonant circuit delivering power and cooling water for the IPGs. Furthermore, both the tube and the coil are surrounded by the tube cooling, which protects the quartz tube from overheating. The water and an additional cage around the generator serve as an rf-radiation protection shield. The length of IPG4 is about 0.4 m (with nozzle). IPG5 is an advanced design where reducing the distance between plasma and coil in turn further reduces the coupling losses [5].

3. Measurement techniques

3.1. Cavity calorimeter

A cavity calorimeter has been developed in order to determine the thermal plasma power in the PWK3 vacuum chamber (Fig. 5) [11]. The working principle is easy. The plasma enters the copper cavity, which is shaped like a cone, through a hole. The diameter of the hole is 120 mm, which is roughly 25% bigger than the usual plasma beams. The distance between the calorimeter and the plasma outlet of the IPG is about 100 mm. This is necessary because smaller distances can result in retroactions that manipulate the discharge behavior of the IPG [5]. Copper is used because of its very high specific heat conductivity and to its high catalysis. The copper walls are heated up through radiation, convection and recombination. The cavity is equipped with spiral copper tubes that guide the water that cools the copper wall.

https://doi.org/10.1017/S0022377807006927 Published online by Cambridge University Press

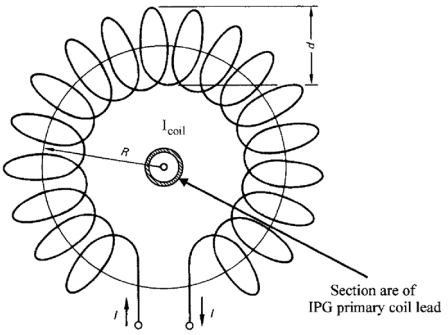


Figure 6. Scheme of the Pearson ring coil, mounted on the IPG coil conductor.

With the measured cooling water exit temperature, the cooling water inlet temperature and the cooling water flow rate the plasma power can be determined:

$$P_{\mathrm{cal}} = \rho_{\mathrm{W}} c_{\mathrm{p,W}} \dot{V}_{\mathrm{W}} (T_{\mathrm{out}} - T_{\mathrm{in}}) + \Delta P. \tag{7}$$

Here ρ_{W} is the density of the cooling water, $\dot{V}_{\mathrm{W}}$ is the cooling water volume flow rate, $c_{\mathrm{p,W}}$ is the heat capacity, T_{out} is the cooling water outlet temperature and T_{in} is the cooling water inlet temperature. The parameter ΔP characterizes power losses owing to the temperatures and velocities of the hot gas leaving the calorimeter's outlet. The corresponding kinetic power can be estimated using equilibrium models for the enthalpy together with the measured gas temperatures and mass flow rates [5].

Correspondingly a total efficiency can be defined as

$$\eta_{\mathrm{tot}} = \frac{P_{\mathrm{cal}}}{P_{\mathrm{A}}}. \tag{8}$$

In addition, a mean specific enthalpy can be calculated:

$$\bar{h} = \frac{P_{\mathrm{cal}}}{\dot{m}} = \eta_{\mathrm{tot}} \frac{P_{\mathrm{A}}}{\dot{m}}. \tag{9}$$

Here, P_{A} is the anode (plate) power and $\dot{m}$ is the plasma generator's working gas mass flow rate.

3.2. Coil current and frequency measurement devices

The coil currents cannot be measured with a connected resistor as the powers and frequencies are too high. Hence, measurement systems had to be found to determine the coil current via the IPG-coil's magnetic field.

3.3. Modified Pearson 6247 current transformator

Figure 6 depicts the schematic view of the current monitor mounted around the IPG conductor. The position of the current monitors used in this kind of investigation is shown in Fig. 7. Measurements with Pearson 6247 have to be performed carefully as the kernel of the device is heated up due to magneto-restriction.

Therefore, the system was modified. Apart from the coil itself and the kernel all metallic housing parts were removed. Both coil and kernel were encapsulated with epoxy resin. The maximum permissible measurement period can be estimated with the help of the manufacturer's data. Having a maximum effective coil current of

https://doi.org/10.1017/S0022377807006927 Published online by Cambridge University Press

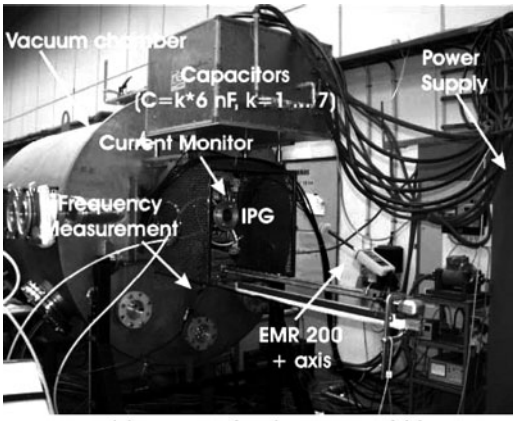


Figure 7. Facility PWK3 with EMR-200 and related measurement techniques.

1.5 kA (I_{eff}), the output signal is 5 mV A^{-1} (internal resistance 10 Ω). The maximum surge current is 100 kA and the current–time product is 20 As. The dissipated heat is proportional to the time integral of $I^2(t)$. Multiplying the surge current with the current–time product and dividing the result by the squared effective current yields the maximum measurement period:

$$t \leqslant \frac{\hat{I}_{\max}(It)_{\text{zul}}}{I_{\text{eff}}^2} = \frac{2 \cdot 10^6 \ A^2 s}{I_{\text{eff}}^2}. \tag{10}$$

Using the maximum effective current, (10) leads to a maximum measurement period of 0.9 s. Typical PWK3-IPG coil currents are around 0.4 to 0.7 kA leading to 13 and 4 s, respectively.

3.4. HOKA: measurement of coil current

Magnetic coil current measurements were performed in order to qualify the developed theory, and resulted in H_{coil} using the transformer equation. The advantage of the new sensor, which was developed by Herdrich [5] and Karrer et al. [33], is its stationary application, i.e. at high power it lasts up to 10 min before it is heated up to ∼340 K, whereas measurements with the Pearson sensor can be performed for only several seconds before overheating is reached. This is made possible by the (coreless) Rogowski coil (see Fig. 6). The losses due to re-magnetization are avoided. The drawback of low signal strength demands a subsequent amplification. The outgoing voltage signal was recorded on a Kontron WW700 transient recorder with a time resolution of $\Delta t = 2.5 \times 10^{-7}$ s in order to measure current signals with a frequency of ∼300 Hz. The conversion factor 1 V = 575 A was determined by fitting the results to calibrated Pearson data, thus obtaining the effective coil current over the anode voltage.

3.5. EMR-200: measurement of electro-magnetic fields

EMR-200 is a flexible system to measure electro-magnetic fields [5]. It can be equipped with different types of probes such that both electric and magnetic fields can be measured in a wide frequency range. Besides the aspect of the facility's safety requirements there is also the possibility of observing secondary effects such as, e.g., damping effects due to the plasma fields that counteract the original

https://doi.org/10.1017/S0022377807006927 Published online by Cambridge University Press

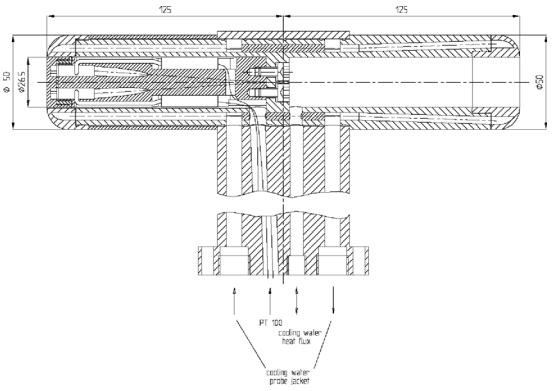


Figure 8. Scheme of steady-state heat flux and Pitot pressure double probe.

coil fields. In spite of the near-field conditions (the Fraunhofer region begins at about 71 m with $f = 670$ kHz), coil currents can be correlated with the measured field strengths as long as defined positions where the field is measured are used consistently. Therefore, a quick indirect measurement of the coil current is possible using EMR-200.

Different types of probes can be attached to the base of the device. The so-called electric field probe type 8 can measure in the frequency region between 100 kHz and 3 GHz, enabling the measurement in the relevant frequency range (Fig. 3). Besides this probe, two more probes to measure magnetic field strengths are in use. The H-field probe type 12 can measure magnetic fields between 300 kHz and 30 MHz. The type 13 probe can measure between 3 kHz and 3 MHz. The sensors have a size of roughly 40 mm which limits the spatial resolution.

Measurements of axial profiles were performed using an electrically driven rail system attached to the cage of the IPG (see Fig. 7). The device was mounted such that the sensors were along the center axis of the IPG.

An optical incremental encoder is used to measure the precise position of the sensor system which is read out together with the sensor signal using a computer program. The middle of the IPG's coil is used as the geometric reference. Finally, the system delivers effective values of the three spatial components (x, y, z) of the field considered.

3.6. Probe measurements

3.6.1. Steady-state heat flux/Pitot pressure probe. The steady state heat flux is measured on an insert which can easily be changed. Usually, copper inserts are used as a reference. For the steady-state case, the flow rate through the insert $\dot{V}$ and the temperature difference of the incoming and outgoing water $(T_{\text{out}} - T_{\text{in}})$ are measured, the latter by electrically insulated and shielded resistance thermometers Pt100. The heat flux per unit area is then given by

$$\dot{q} = \frac{c_{\text{p,W}} \rho_W \dot{V}_W (T_{\text{out}} - T_{\text{in}})}{A}, \tag{11}$$

where $c_{\text{p,W}}$ is the heat capacity of water, ρ_{W} is the water density and A is the surface area of the probe exposed to the plasma. Figure 8 shows a drawing of the steady state heat flux and Pitot pressure double probe that were used [5]. The heat flux

https://doi.org/10.1017/S0022377807006927 Published online by Cambridge University Press

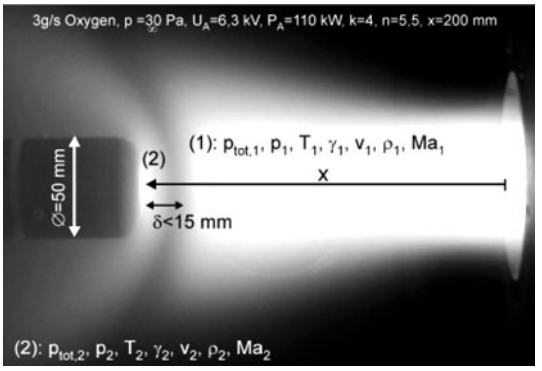


Figure 9. Supersonic flow condition in PWK3 (IPG3) with notation for flow parameters.

sensor has a diameter of 26.5 mm according to the European standard geometry for heat shield material samples. On the right-hand side the Pitot pressure hole can be seen. The same diameter was used for the investigations. However, a variation of diameter can be performed by exchanging the modular insert for the pressure hole.

The Pitot pressure enables statements on the flow condition, in particular on the Mach number of the plasma flow using (subsonic)

$$M_{a1} = \sqrt{\frac{2}{\gamma - 1}\left[\left(\frac{p_{\mathrm{tot}}}{p_{\mathrm{amb}}}\right)^{(\gamma-1)/\gamma} - 1\right]}. \tag{12}$$

The notation used is shown in Fig. 9 ($p_1 \approx p_{\mathrm{amb}}$).

For the supersonic case

$$\frac{(\gamma+1)^{\gamma+1} Ma_1^{2\gamma}}{2\gamma Ma_1^2 - \gamma + 1} = 2^{\gamma}\left(\frac{p_{\mathrm{tot}}}{p_{\mathrm{amb}}}\right)^{\gamma-1} \tag{13}$$

is used, where γ is the adiabatic coefficient and Ma_1 is the Mach number. Both equations assume constant heat capacities. The static pressure is assumed to be the ambient pressure in the vacuum chamber. Hence, the measured pressure ratio leads to the Mach number in the form

$$Ma = f\left(\frac{p_{\mathrm{Pitot}}}{p_{\mathrm{amb}}}, \gamma\right). \tag{14}$$

The resulting Mach numbers are illustrated in Fig. 10. The full symbols show the interval calculated using (12), while the open symbols were calculated with (13).

3.6.2. Wedge probe for Mach number determination. The design of the wedge probe [5] enables both the static pressure and the Mach number to be determined as all shock waves may be attached to pointed bodies. The water-cooled wedge is placed in the supersonic plasma flow as shown in Fig. 11.

The sharp edge of the wedge is the origin of Mach lines that are at an angle α to the horizontal such that the Mach number can be calculated using

$$Ma = [\sin(\alpha)]^{-1}. \tag{15}$$

https://doi.org/10.1017/S0022377807006927 Published online by Cambridge University Press

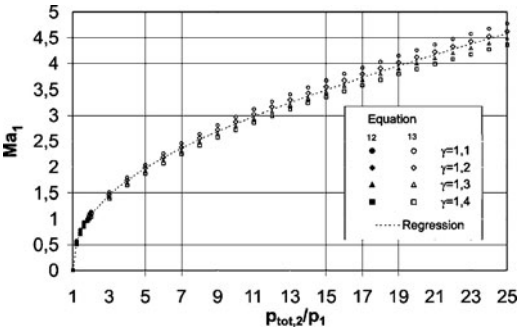


Figure 10. Ma_1 depending on pressure ratio $p_{\mathrm{tot},2}/p_1$.

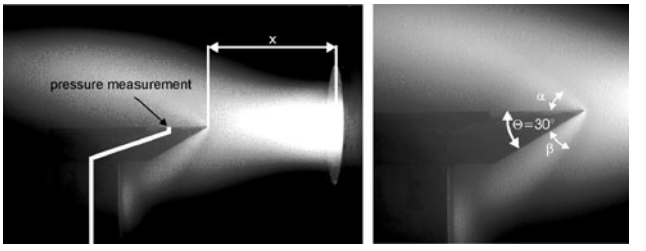


Figure 11. IRS wedge probe in oxygen plasma flow, IPG3, $f_{5,5;4} \approx 0.64$ MHz, $p_{\mathrm{amb}} \approx 40$ Pa, $x = 150$ mm; right: magnified.

Analog behavior is provided for the lower side of the wedge probe where the angle β depends on the wedge angle Θ (here: 30°) and on the adiabatic coefficient γ:

$$\cot(\Theta) = \tan(\beta)\left[\frac{(\gamma+1)Ma_1^2}{2(Ma_1^2\sin^2(\beta)-1)} - 1\right]. \tag{16}$$

However, the analysis of shock polars shows that a shock wave can be formed in front of the probe provided that the Mach number becomes too low. For wedges the detachment of the shock wave strongly depends on the wedge angle Θ. In addition, it also depends on γ. For 30°, as used in this investigation, the detachment appears for [5]

$$Ma_1|^{\Theta=30^\circ}_{\gamma=1,1-1,2} \leqslant 2.05,\ldots,2.2. \tag{17}$$

Under these conditions one has $\beta \approx 65°$–$66°$ and $\alpha \approx 29.2°$–$27°$ ($\gamma = 1.2$–1.1), i.e. that the direct measurement of the Mach numbers using (15) and (16) is limited to Mach numbers larger than the values shown by (17). Of course, photographs of detached shock waves can also be consulted to determine the Mach number if a geometry comparison with numerically simulation is used.

4. Behavior of an IPG based on one-dimensional modeling

Models describing the coupling behavior of IPG have been previously published (see also the introduction section in [5]). However, parameters such as the coil current, field strengths and plasma power enable an analysis of the operational behavior of IPGs. With simple models, existing interpretations can be confirmed and, in addition, explanations for the operational behavior can be found. Furthermore,

https://doi.org/10.1017/S0022377807006927 Published online by Cambridge University Press

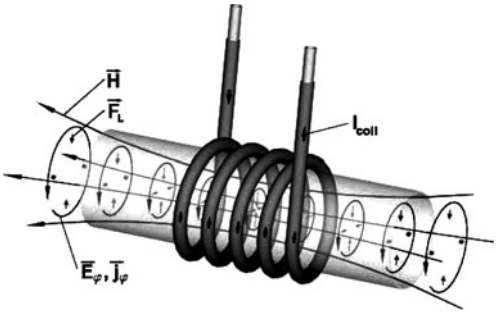


Figure 12. Electrodynamic behavior of an IPG.

MHD effects may explain certain performances of the IPG. Figure 12 shows the electrodynamic behavior of an IPG.

In order to establish algebraic solutions for the complex Maxwell equations, a set of assumptions and simplifications has to be kept as follows.

(a) A very simple version of Ohm's law is used:

$$\mathbf{j}_\varphi = \sigma \mathbf{E}_\varphi . \tag{18}$$

(b) The electrical conductivity of the plasma is assumed to be constant in the considered volume ($\sigma = \sigma_{\text{eff}}$).

(c) End effects of the coil are neglected.

(d) Electrodynamic parameters are sinusoidal.

(e) Radial heat conductivity losses in the tube are not considered.

(f) All sizes in the IPG tube are rotationally axisymmetric.

(g) The dielectric displacement (current) is neglected. This is reasonable as the wavelength ($\lambda = c/f$) is in the order of magnitude of 10^2 m while the IPG geometry is approximately 10^{-1} m, see [5]. Therefore, the second Maxwell equation becomes

$$\text{rot } \mathbf{H} = \mathbf{j}. \tag{19}$$

(h) The plasma is assumed to be quasi-neutral. The fourth Maxwell equation becomes

$$\text{div}(\mathbf{E}) = 0. \tag{20}$$

By eliminating E using the Maxwell equations and the simplifications (a) to (f) one yields the Helmholtz equation:

$$\Delta \mathbf{H} - i \underbrace{(\mu_0 \mu_\text{r} \omega \sigma)}_{\text{inductive term}} \mathbf{H} + \underbrace{(\mu_0 \varepsilon_0 \varepsilon_\text{r} \omega^2)}_{\text{dielectric term}} \mathbf{H} = 0. \tag{21}$$

An analysis of (21) with respect to the significance of the dielectric term shows that the coefficient $\mu_0 \varepsilon_0 \varepsilon_\text{r} \omega^2$ is negligible within the concerned frequency range (Fig. 3). Equation (19) is, therefore, applicable.

https://doi.org/10.1017/S0022377807006927 Published online by Cambridge University Press

Solving the equation system using an analog procedure where H is eliminated using (20) and expressing the resulting equations in cylindrical coordinates leads to

$$\frac{\partial^2 H_z}{\partial r^2} + \frac{1}{r}\frac{\partial H_z}{\partial r} - i\frac{2}{\delta^2}H_z = 0, \tag{22}$$

$$\frac{\partial^2 E_\varphi}{\partial r^2} + \frac{1}{r}\frac{\partial E_\varphi}{\partial r} - \left(\frac{1}{r^2} + i\frac{2}{\delta^2}\right)E_\varphi = 0. \tag{23}$$

Here, δ is the attenuation equivalent (skin depth) which can also be derived directly from (21):

$$\delta = \sqrt{\frac{2}{\omega\mu_0\sigma}}. \tag{24}$$

This well-known parameter is often referred to as depth of penetration. However, it has to be explained that this consideration has its origin in the analysis of IPGs with very high d/δ or very low δ/R ratios where (21)–(23) can be simplified by an approximation leading to exponential functions for j_φ, H_z and E_φ (see [34]). Assuming the magnetic field strength at the tube wall ($r = R = d/2$) to be H_{coil}, one obtains the solution

$$H_z = H_{\text{coil}} J_0^{-1}\left(\sqrt{\frac{-i}{2}}\frac{d}{\delta}\right) J_0\left(\sqrt{-2i}\frac{r}{\delta}\right), \tag{25}$$

$$E_\varphi = H_{\text{coil}}\frac{\sqrt{-2i}}{\delta\sigma} J_0^{-1}\left(\sqrt{\frac{-i}{2}}\frac{d}{\delta}\right) J_1\left(\sqrt{-2i}\frac{r}{\delta}\right), \tag{26}$$

and with (18)

$$j_\varphi = H_{\text{coil}}\frac{\sqrt{-2i}}{\delta} J_0^{-1}\left(\sqrt{\frac{-i}{2}}\frac{d}{\delta}\right) J_1\left(\sqrt{-2i}\frac{r}{\delta}\right). \tag{27}$$

Here, J_0 and J_1 are first kind Bessel functions of zeroth and first order. Equations (25)–(27) can be re-written by using some help functions deduced in Appendix A. Exemplarily, for H_z and E_ϕ this leads to

$$H_z\left(\frac{\delta}{R}, r\right) = H_{\text{coil}}\frac{F(r) + iG(r)}{F(\delta/R) + iG(\delta/R)} \tag{28}$$

and

$$E_\varphi\left(\frac{\delta}{R}, r\right) = H_{\text{coil}}\frac{\sqrt{-2i}}{\delta\sigma}\frac{K(r) + iL(r)}{F(\delta/R) + iG(\delta R)}. \tag{29}$$

All deduced help functions principally depend on the ratio of the skin depth δ to a radius r or R. Hence, varying the attenuation factor δ/R with a constantly assumed plasma radius R, immediately reduces the dependency of δ/r on the radial position r. Thus, interesting quantities such as the radial distribution of field damping and phase displacement depending on this attenuation factor can be calculated. Exemplarily, this leads to

$$\frac{|H_z|}{H_{\text{coil}}} = \frac{\sqrt{[F(r)F(\delta/R) + G(r)G(\delta/R)]^2 + [F(\delta/R)G(r) - F(r)G(\delta/R)]^2}}{F^2(\delta/R) + G^2(\delta/R)} \tag{30}$$

and

$$\Phi = \arctan\frac{F(\delta/R)G(r) - F(r)G(\delta/R)}{F(r)F(\delta/R) + G(r)G(\delta/R)}. \tag{31}$$

https://doi.org/10.1017/S0022377807006927 Published online by Cambridge University Press

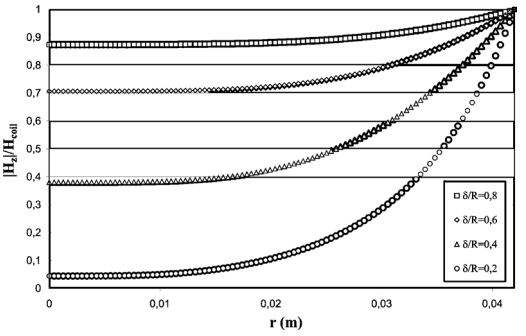


Figure 13. Radial magnetic field distribution for different attenuation factors and $R = 0.042$ m.

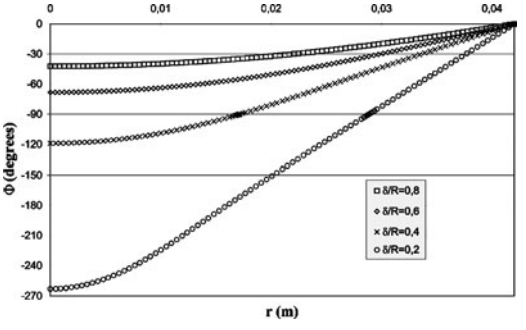


Figure 14. Radial phase displacement for different attenuation factors and $R = 0.042$ m.

The distributions for different attenuation factors are depicted in Figs 13 and 14, where the effective plasma radius R has been approximated by the inner tube diameter.

Obviously, the lower the attenuation factor, i.e. the stronger the skin effect, the stronger the field damping and phase displacement. This complies with what was expected. Accordingly, for the electric field distribution one obtains

$$\frac{|E_\varphi|}{\sqrt{2}H_{\text{coil}}/(\delta\sigma)} = \frac{\sqrt{2}}{F^2(\delta/R) + G^2(\delta/R)} \cdot \{[K(r)F(\delta/R)]^2 + [K(r)G(\delta/R)]^2 + [L(r)G(\delta/R)]^2 + [L(r)F(\delta/R)]^2\}^{1/2}. \tag{32}$$

The result is depicted in Fig. 15. Again, the exponential behavior is reproduced for strong attenuation. The behavior appears to be linear for low attenuation which is a consequence of the almost constant magnetic field distribution for high δ/R ratios. Here, the lower the attenuation, the stronger the deviation from maximum field strength at the boundary. Over the radius, maximum field strength is reached for $\delta/R = 0.6$ which corresponds to the optimum point identified in the following section.

https://doi.org/10.1017/S0022377807006927 Published online by Cambridge University Press

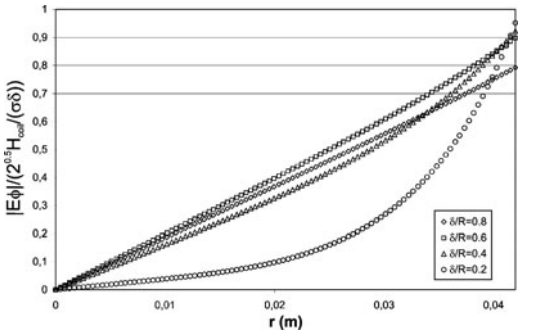


Figure 15. Radial electric field distribution for different attenuation factors and $R = 0.042$ m.

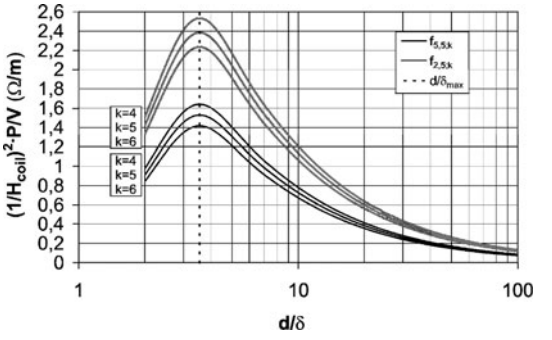


Figure 16. Mean volumetric power density normalized by H_{coil}^2 over d/δ for $f_{2.5;k}$ and $f_{5.5;k}$.

4.1. Volumetric power density

With (18) and (26) the volumetric power density is given [5]. Integrating this over the volume, the induced plasma power

$$P_i = 2\mu_0 fl(\pi\delta H_{\text{coil}})^2 \cdot \text{Re}\left\{\sqrt{-i}\frac{d}{\sqrt{2}\delta}J_1\left(\sqrt{-i}\frac{d}{\sqrt{2}\delta}\right)J_0^{-1}\left(\sqrt{-i}\frac{d}{\sqrt{2}\delta}\right)\right\} \tag{33}$$

is obtained. Dividing (32) by the volume leads to the mean volumetric power density:

$$\frac{P_i}{V} = 2\mu_0\omega H_{\text{coil}}^2\left(\frac{d}{\delta}\right)^{-1} \cdot \text{Re}\left\{(i+1)J_1\left(\sqrt{-i}\frac{d}{\sqrt{2}\delta}\right)J_0^{-1}\left(\sqrt{-i}\frac{d}{\sqrt{2}\delta}\right)\right\}. \tag{34}$$

Figure 16 depicts the curves resulting from (34) under variation of frequency. Here, the investigated coils for $n = 2.5$ and 5.5 are analyzed. Besides the increase of the induced power with increasing frequency, the model shows a maximum for $d/\delta \approx 3.6$ which is equivalent to $\delta/R \approx 0.57$ and almost independent from frequency. This maximum is also provided for (33). The importance of this result has to be emphasized as an optimization of the IPG with respect to a maximum induced plasma power seems to be possible.

https://doi.org/10.1017/S0022377807006927 Published online by Cambridge University Press

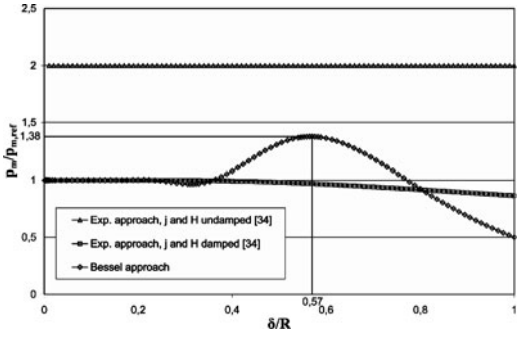


Figure 17. Normalized distribution of magnetic pressure (in relation to $p_{\mathrm{m,ref}}$) depending on δ/R with respect to the Bessel and the exponential approach.

4.2. Magnetic pressure

The field distribution functions resulting from the one-dimensional Bessel model can be used to investigate the pinch effect, which describes a plasma constriction based on electromagnetic forces, e.g. in the case that magnetic pressure exceeds the plasma pressure or even reaches a non-negligible magnitude in the context of plasma interaction. The so-called theta pinch, named after the international notation for the azimuthal direction of plasma current, was investigated. Given the simplified momentum equation

$$\nabla p = \mathbf{j} \times \mathbf{B} \tag{35}$$

with $p = p(r)$ for an inviscid, quasi-neutral, static, steady-state plasma without gravitational influences, the one-dimensional formulation for cylindric geometry can be derived easily. Usually, the unknown current density is eliminated by a simplification of Ampere's law, thus obtaining

$$p_{\mathrm{m}} = \frac{\mu_0 H_z^2}{2} = p_{\mathrm{m,ref}} \tag{36}$$

after integrating over r. This term depends on the magnetic field only and will serve as a reference quantity. With (25) and (27) and $\mu_r = 1$ from (35) one obtains

$$p_{\mathrm{m}} = \int_0^R j_\varphi B_z \, dr = \mu_0 H_{\mathrm{coil}}^2 \left(1 - \frac{1}{J_0^2(aR)}\right). \tag{37}$$

Clearly, the result is of complex character although the physically effective quantity is the real part:

$$p_{\mathrm{m}}\left(\frac{\delta}{R}\right) = \mu_0 H_{\mathrm{coil}}^2 \left(1 - \frac{C(\delta/R)}{C^2(\delta/R) + D^2(\delta/R)}\right). \tag{38}$$

Here, the deduced help functions were applied. The distribution of $p_{\mathrm{m}}/p_{\mathrm{m,ref}}$ over δ/R is depicted in Fig. 17.

The exponential approach without field damping yields excessive values, whereas the exponential approach with field damping yields the same results as the Bessel approach at high power, i.e. strong skin effect ($\delta/R \to 0$). Considering the Bessel approach curve, three facts should be pointed out.

1. There is a maximum at $\delta/R \approx 0.57$. This value is identical with the maximum depicted in Fig. 16 ($d = 2R$).

https://doi.org/10.1017/S0022377807006927 Published online by Cambridge University Press

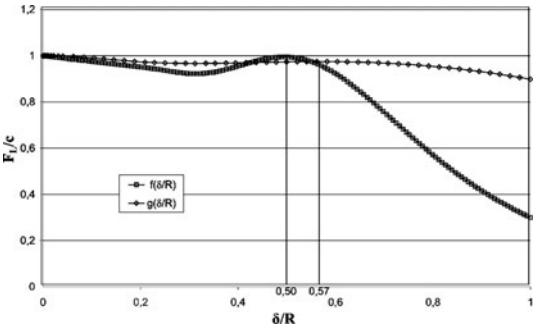


Figure 18. Qualitative distribution of the radial Lorentz force depending on δ/R.

2. For strong field attenuation ($\delta/R \leqslant 0.2$) the magnetic pressure passes into $p_{\mathrm{m,ref}}$. This shows that the known term for the magnetic pressure (36) is valid for strong field attenuation only.

3. The existence of a maximum shows that there is in principle the possibility to optimize over δ/R with respect to the magnetic pressure, the induced power and thermal tube load.

Figures 16 and 17 show a correlation between power induction, plasma constriction and the tube cooling phenomenon.

4.3. Lorentz force

The integral Lorentz force can be calculated generally by the integration of the Lorentz force density over the volume:

$$\mathbf{F}_{\mathrm{L}} = \mathrm{Re}\left(\int_V \mathbf{f}_{\mathrm{L}}\, dV\right) = \mathrm{Re}\left(\int_V (\mathbf{j} \times \mathbf{B})\, dV\right). \tag{39}$$

Applying the proper help functions $A(\delta/R)$, $B(\delta/R)$, etc. gives

$$F_{\mathrm{L}}\left(\frac{\delta}{R}\right) = c\left(1 - \frac{A(\delta/R)C(\delta/R) + B(\delta/R)D(\delta/R)}{C(\delta/R)^2 + D(\delta/R)^2}\right) = cf(\delta/R) \tag{40}$$

with $c = -Rl\pi\mu_0 H_{\mathrm{coil}}^2$ which is equivalent to the maximum Lorentz force. The result is negative because of the inwardly directed force. The distribution of f over δ/R is depicted in Fig. 18, which shows a maximum at $\delta/R \approx 0.5$.

The other maximum at $\delta/R \to 0$ is academic and not reached in the context of partially ionized (low-temperature) plasmas.

Alternatively, one can calculate the radial Lorentz forces for strong attenuation [5]. This assumption leads to the exponential approach for the integral plasma current

$$I_{\mathrm{Pl,eff}} = \frac{j_{\max} l_{\mathrm{coil}} \delta}{\sqrt{2}}(1 - e^{-R/\delta}) \approx j_{\mathrm{eff}} l_{\mathrm{coil}} \delta. \tag{41}$$

The radial Lorentz force is then

$$F_{\mathrm{L}} = c \cdot \left(\frac{1 - (\delta/2R)(1 - e^{-2R/\delta})}{(1 - e^{-R/\delta})^2}\right) = c \cdot g\left(\frac{\delta}{R}\right). \tag{42}$$

The expression $g(\delta/R)$ is also depicted in Fig. 18. In the case of the Lorentz force, the exponential approach is quite a good approximation. The optimum attenuation

https://doi.org/10.1017/S0022377807006927 Published online by Cambridge University Press

factor is shifted 'only' to $\delta/R \approx 0.57$. This solution can be further simplified to

$$F_{\mathrm{L}} \approx -\frac{\pi}{2}\mu_0 \frac{d}{l} I_{\mathrm{Pl,eff}}^2 = -\frac{P_{\mathrm{Pl}}}{4\omega\delta} = -\frac{P_{\mathrm{Pl}}}{4\omega R \cdot (\delta/R)}. \tag{43}$$

Equation (43) allows statements on the MHD behavior of an IPG depending on the integral parameters P_{Pl}, $I_{\mathrm{Pl,eff}}$, the frequency and the skin depth δ. As can be easily seen, the Lorentz force increases with P_{Pl} as it can be expected that δ decreases simultaneously, see also (24). Therefore, (43) is of significance as the power dependency of stabilizing effects can be illustrated. Having an efficient inductive coupling fulfilling the inequality $\delta < R$, (43) can be used to estimate F_{L}, i.e. $F_{\mathrm{L}}/P_{\mathrm{Pl}} > 1/(4 \cdot \omega R)$.

The relevance of MHD effects for the operational behavior of the IPG can additionally be demonstrated by considering of the dimensionless Stewart and magnetic Reynolds numbers as was presented in [42] yielding $St \approx 1$ and $R_{\mathrm{m}} \approx 7$.

5. Characteristics of the plasma

Assuming thermo-chemical equilibrium, both plasma composition and enthalpy can be calculated based on the law of mass action and the classical approaches for the different energy terms, e.g. for the homonuclear molecule oxygen. Different references were used to confirm the model, e.g. the law of mass action was evaluated on the basis of tables, thermodynamic data and statistical thermodynamics. In addition, the results were compared with more complex numerical equilibrium models of Andriatis and Sokolowa, see [5], and showed a very good correspondence, e.g. for the molar fractions of both atomic oxygen, molecular oxygen and the ionization degree that has been calculated using the Eggert–Saha equation.

The energies can be derived using the calculated molar fractions. For the energy of a molecule A_2 one obtains

$$e_{A_2} = \frac{3}{2}\Re T_{\mathrm{trans}} + \Re T_{\mathrm{rot}} + \Re \frac{\theta}{e^{\theta/T_{\mathrm{vib}}} - 1}, \tag{44}$$

with R a gas constant and Θ the specific vibrational temperature of oxygen (2239 K). The three temperatures are considered to be in equilibrium. The energy of an atom is

$$e_A = \frac{3}{2}\Re T_{\mathrm{trans}} + \frac{D}{2}, \tag{45}$$

with D as dissociation energy. Finally, the energy contribution of the electrons is represented by

$$e_{\mathrm{e}} = \tfrac{3}{2}\Re T_{\mathrm{e}} + W_{\mathrm{i}}, \tag{46}$$

where W_{i} is the ionization energy. The specific total energy is, therefore,

$$e_{\mathrm{tot}} = \psi_{A_2} e_{A_2} + \psi_A e_A + \psi_{\mathrm{e}} e_{\mathrm{e}}. \tag{47}$$

Here, the Ψ_i are the different molar fractions of the species. Assuming that ionization starts after the dissociation is completed, the energy of the quasi-neutral plasma can be calculated algebraically in two intervals:

$$e_{\mathrm{tot}} = (1 - \Delta) e_{A_2} + \Delta e_A, \tag{48}$$

$$e_{\mathrm{tot}} = (1 - 2\psi_{\mathrm{e}}) e_A + \psi_{\mathrm{e}} e_{\mathrm{i}} + \psi_{\mathrm{e}} e_{\mathrm{e}}. \tag{49}$$

Here, Δ is the dissociation degree (Ψ_A) and Ψ_{e} is the molar fraction of the electrons.

https://doi.org/10.1017/S0022377807006927 Published online by Cambridge University Press

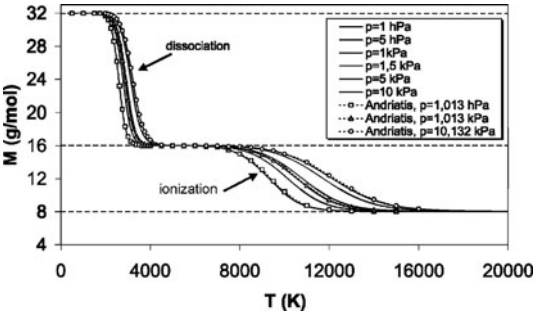


Figure 19. Mean molar mass of oxygen versus temperature and pressure; compared with Andriatis and Sokolowa.

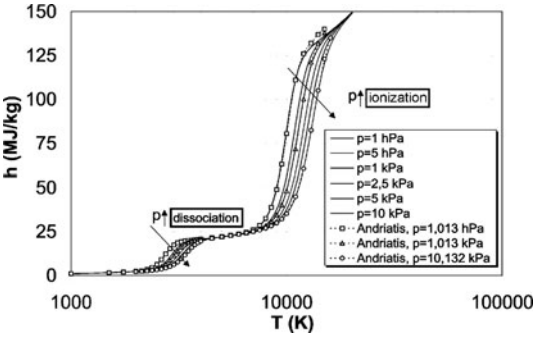


Figure 20. Mass specific enthalpy of oxygen versus temperature and pressure; compared with Andriatis and Sokolowa.

For the specific enthalpy one obtains

$$h = e_{\mathrm{tot}} + \Re T. \tag{50}$$

Together with the mass specific kinetic energy the mass specific enthalpy is

$$h_{\mathrm{tot}} = \frac{e_{\mathrm{tot}}(T)}{M(p,T)} + \frac{\Re T}{M(p,T)} + \frac{v^2}{2}, \tag{51}$$

with M the mean molar mass calculated using the law of mass action. Figure 19 depicts the mean molar mass for oxygen and Fig. 20 shows the mass specific enthalpies, both compared with the data of Andriatis and Sokolowa; see also [5].

Good agreement can be seen. In [5] the same model was used and qualified for nitrogen. Here, a quite good correspondence was seen as well. In both figures, the pressure dependency of the dissociation and the first ionization regime can be seen very well.

Having the equilibrium molar fractions, the electrical conductivity σ can be calculated using the relevant cross sections [5]:

$$\sigma = \frac{3}{8}\sqrt{\frac{\pi}{2}}\frac{1}{\sqrt{kT_{\mathrm{e}}m_{\mathrm{e}}}}\frac{\alpha Q_{\mathrm{e-i}}}{\alpha Q_{\mathrm{e-i}} + (1-\alpha)Q_{\mathrm{e-0}}}. \tag{52}$$

Here, α is the ionization degree ($\alpha = \Psi_{\mathrm{e}}/(1-\Psi_{\mathrm{e}})$), $Q_{\mathrm{e-0}}$ is the collision cross section between electrons and neutral species and $Q_{\mathrm{e-i}}$ is the Gvosdover cross section

https://doi.org/10.1017/S0022377807006927 Published online by Cambridge University Press

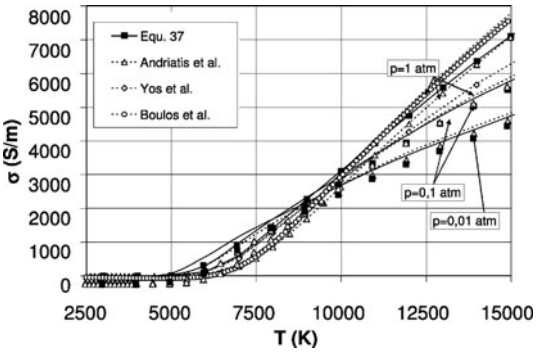


Figure 21. Electric conductivity for oxygen, $p = 0.01$, 0.1 and 1 atm.

(charged-charged). The data for Q_{e-0} have been taken from different references, the Gvosdover cross section has been calculated based on Sleziona's model [35].

Figure 21 shows literature results of the analysis. It has to be emphasized that data for pure oxygen are poor. In 5 a further comparison for nitrogen has been made with a pretty good agreement which confirms the present approach.

6. Measurements and analysis

Measurement results are presented and analyzed based on the compiled models.

6.1. Characterization of the IPG

The design of the IRS-IPGs (IPG3, IPG4, IPG5) allows for steady-state operation in wide power ranges. In addition, ignition tools or starting gases such as argon are not required. Therefore, the power-specific behavior can be investigated. In comparison with other existing systems [22, 36], the potential of parameter variation is larger such that the dependency of typical parameter can be investigated systematically.

In Fig. 22 the facility-related anode power set of characteristic curves is shown for IPG3 with $f_{5.5;4} \approx 0.64$ MHz (Fig. 3) for different oxygen mass flow rates. The wall thickness of the tube is $t \approx 2.3$ mm. The powers shown have been measured in steady-state mode during long measurement periods. This qualifies IPG3 for basic investigations such as analysis of TPS catalysis and oxidation behavior using pure oxygen plasmas [28].

Figure 23 depicts the corresponding tube pressures. It can be seen that depending on power and mass flow rate up to 19 hPa are reached. Anode powers over 60 kW lead to pressures larger than 9 hPa. Such high values in combination with low ambient pressures in PWK3 lead to supersonic flow conditions.

Depending on the power, three different operational states can be observed. The transitions between these discharge modes are discrete.

(i) At low power levels a weakly glowing plasma can be observed. More detailed investigations together with measurements of the radial intensity histories in the IPG show that this mode is a capacitive discharge mode [3, 5].

(ii) As the power is increased, a sudden transition followed by a new discharge mode appears. With the transition there is an evident increase in the plasma

https://doi.org/10.1017/S0022377807006927 Published online by Cambridge University Press

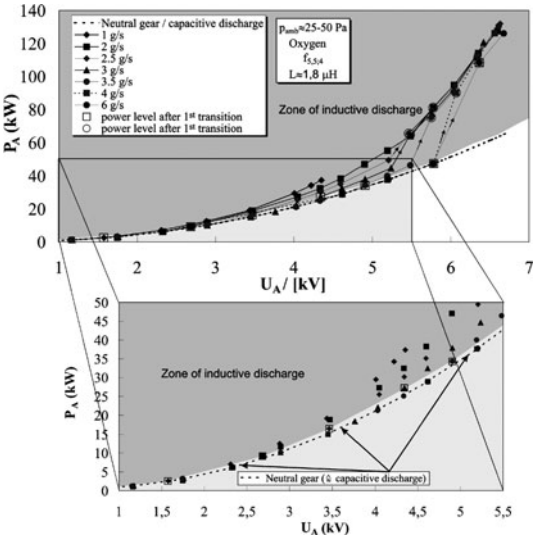


Figure 22. Set of characteristic anode power curves over anode voltage for oxygen plasma with $f_{5.5;4}$ and tube wall thickness $t = 2.3$ mm, variation of mass flow rate.

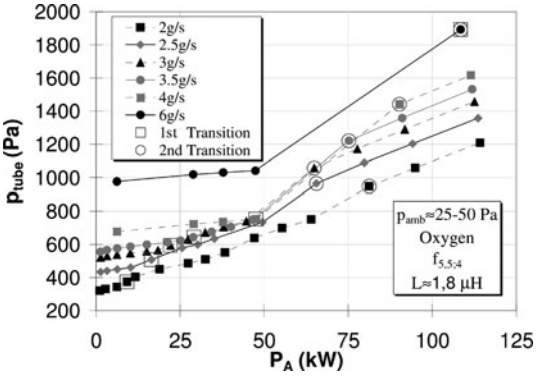


Figure 23. Tube pressure over anode power for oxygen plasma with $f_{5.5;4}$ and $t = 2.3$ mm, variation of mass flow rate.

intensity. This mode represents the inductive discharge mode. The transition anode voltage depends on pressure, working gas and frequency. Apart from the control anode voltage, all relevant operational parameters change discretely with the transition. In Fig. 22 the first power levels of the inductive mode are marked by a square. It can be seen that the gradient of the pressure histories increases with the first transition. In addition, the transition shifts to higher powers with increasing mass flow rates.

(iii) The second transition marked in Fig. 22 by the arrows is accompanied by stronger changes of parameters such as, e.g., anode power and tube pressure. The power in the plasma jumps to a higher level. Simultaneously, the tube cooling power decreases and remains at an almost constant level with further power increase. Figure 23 depicts the behavior of tube pressure. For the

https://doi.org/10.1017/S0022377807006927 Published online by Cambridge University Press

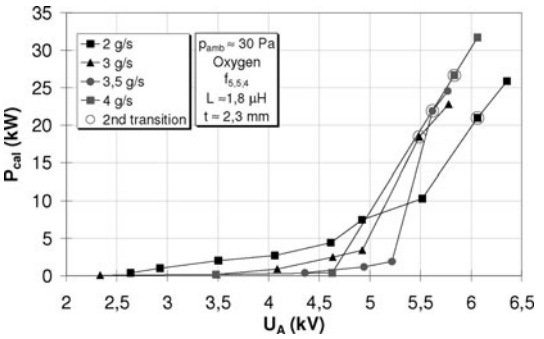


Figure 24. Plasma power over anode voltage for oxygen plasma, variation of mass flow rate.

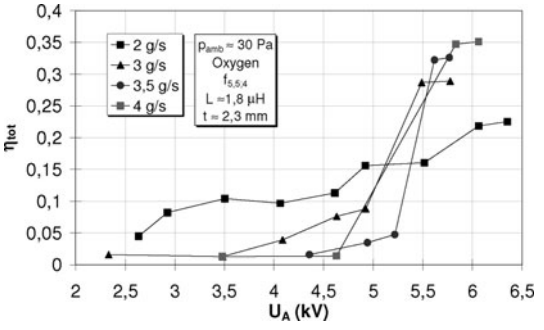


Figure 25. η_{tot} over anode voltage for oxygen plasma, variation of mass flow rate.

condition with 6 g s^{-1} both transitions coincide with each other. This can be explained by the shift of the first transition with increasing mass flow rates.

The corresponding plasma powers measured with the calorimeter in PWK3 are shown in Fig. 24.

Before the inductive mode starts, all mass flow rates share a common curve (see also Fig. 22). Measured powers in the first mode are at the 10^{-1} kW level. This observation can be confirmed by theoretical analysis of the capacitively coupled power [5]. However, at such low powers the accuracy of the calorimeter is low. With the first transition, powers of several kilowatts are detected. They increase with increasing anode voltage. A further increase of the anode voltage leads to a sudden power jump. It has to be emphasized that the transition points cannot be influenced by a variation of the tube cooling power. The strong increase of the plasma power can, therefore, be explained by a sudden increase of the electrical conductivity of the plasma. The transition corresponds with the sudden increase of the anode powers in Fig. 22.

Considering η_{tot} (8) in Fig. 25, the operational behavior becomes even more evident: the efficiency strongly increases with the second transition.

For 2 g s^{-1} this feature occurs less. This observation can be generalized. For 2 g s^{-1} η_{tot} is about 0.22, whereas 3 g s^{-1}, 3.5 g s^{-1} and 4 g s^{-1} lead to η_{tot} values between 0.28 and 0.35. This difference may be explained by the fact that the MHD effects in the tube play a role.

https://doi.org/10.1017/S0022377807006927 Published online by Cambridge University Press

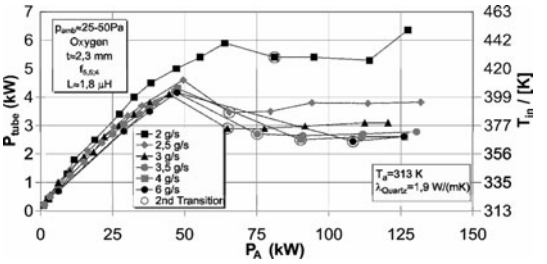


Figure 26. Tube cooling power and quartz tube inner wall temperature over anode power for oxygen plasmas, variation of mass flow rate.

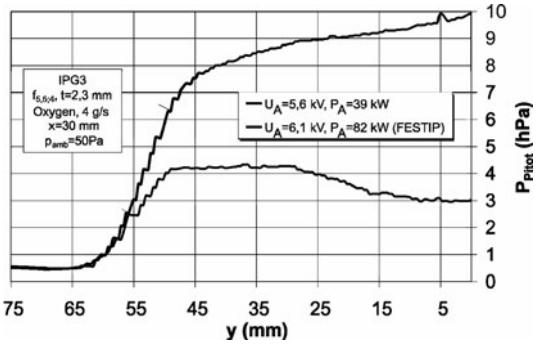


Figure 27. Radial Pitot pressure profiles before and after second transition for mass flow rate 4 g s^{-1}.

In the simultaneously measured tube cooling powers in Fig. 26, it can be seen that the cooling powers decrease although there is an evident increase in the anode power and in turn the plasma power. Finally, increasing P_A in the third discharge mode further has almost no effect on the tube cooling power. Together with the data given in Fig. 24, where there is an evident increase in the corresponding power in the tank, the presumption that the plasma is radially pinched can be made. This can be explained by $\mathbf{j} \times \mathbf{B}$-forces leading to a decrease of the thermal load of the tube wall. The tube cooling powers are stationary. Therefore, the inner tube wall temperatures can be calculated one-dimensionally, see Fig. 26. The temperatures do not increase considerably after the second transition.

In Fig. 27 radial profiles for the Pitot pressure using an oxygen condition with a mass flow rate of 4 g s^{-1} at an operational frequency of 0.64 MHz (5.5-turn coil, four capacitors) are shown before and after the second transition. Here it can be observed that the profile at $U_A = 5.6$ kV, where the discharge is just below the second transition, has a flat maximum at the edge of the plasma jet which is due to the skin effect. For $U_A = 6.1$ kV the situation changes drastically: now a Pitot pressure profile is achieved with a maximum in the center of the plasma jet. Simultaneously, the overall pressure values are significantly higher compared with the $U_A = 5.6$ kV condition. Together with all implications and analytic considerations this result enforces the impression that the second transition is accompanied by significant Lorentz forces that have the pressure increase and the profile change as a consequence.

https://doi.org/10.1017/S0022377807006927 Published online by Cambridge University Press

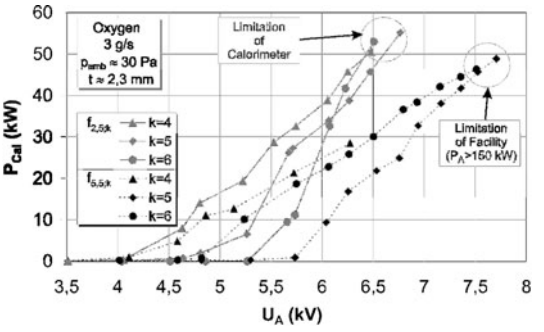


Figure 28. Calorimetric powers versus anode voltage for oxygen, $f_{2.5;k}$ and $f_{5.5;k}$.

With (24) it is found that the skin depth δ decreases owing to the increase of σ which means that thermal power is coupled into a 'cage' that becomes smaller with increasing power. This, however, strengthens the presumption that MHD effects play a role in the observed operational behavior. In addition, (43) can be used to explain this behavior as both increase of total plasma power and decrease of skin depth allow for an increase of the Lorentz force ($F_{\mathrm{L}} \propto P_{\mathrm{Pl}}/\delta$). The strong increase of power with the second transition results in a strong increase of F_{L}. A similar statement applies for the increase of σ. However, such processes need not be one-dimensional so that a combined effect, i.e. Lorentz forces together with stimulated flows, cannot be excluded, as e.g. demonstrated by Boulos et al., see also [5]. With the inequation $F_{\mathrm{L}} > P_{\mathrm{Pl}}/(4\omega R)$ and the plasma powers shown in Fig. 24 the following statements can be made: With the second transition the radial Lorentz forces for 2 g s^{-1} increase at least by a factor of 2, for 3 g s^{-1} at least by a factor of 4.2, for 3.5 g s^{-1} by a factor of 10.8 and for 4 g s^{-1} by a factor of 65.

Figure 28 depicts measured calorimetric powers for 3 g s^{-1} oxygen with $p_{\mathrm{amb}} \approx$ 30 Pa under variation of operational frequency $f_{n;k}$. Basically, the change of n is in high gear, as for $n = 2.5$ evidently higher powers result at comparable facility conditions. Similar behavior is found for the variation of the number of capacitors k ($n = 2.5$) with the exception that $f_{2.5;6}$ intersects with the curves for $f_{2.5;5}$ and $f_{2.5;4}$ between $U_A = 6.1$ and 6.5 kV. For $n = 5.5$ the results are different. However, a trend of increasing powers with increasing frequencies seems to result. This observation is predicted by (33).

With d given, the mean volumetric power density is roughly proportional to the square root of the frequency assuming that H_0 has no frequency dependence. The results show that the coupled power can be increased by more than 50% if adequate frequencies are used. With k = constant. Equation (5) delivers $(f_1/f_2) \approx (n_2/n_1)$ leading to a power ratio of 1.5 in the present case (33). This corresponds well with the results in Fig. 28. As expected, the sensitivity referring to a variation of n is higher in comparison with k.

In Fig. 29 effective coil currents for oxygen, nitrogen and air plasmas depending on the anode voltage are shown. These effective values are derived from high-resolution current measurements using a transient recorder. The filled symbols show three cases, 3 g s^{-1} oxygen, 4 g s^{-1} oxygen and 3 g s^{-1} nitrogen, all of them measured under minimum pressure conditions and at the frequency $f_{5.5;4} \approx 0.64$ MHz.

All histories follow a common curve up to roughly 4.2 kV. For oxygen (3 g s^{-1}) the second transition occurs at about 5 kV. Initially, the current exceeds 0.5 kA; with the third discharge mode the current jumps back to 0.4 kA.

https://doi.org/10.1017/S0022377807006927 Published online by Cambridge University Press

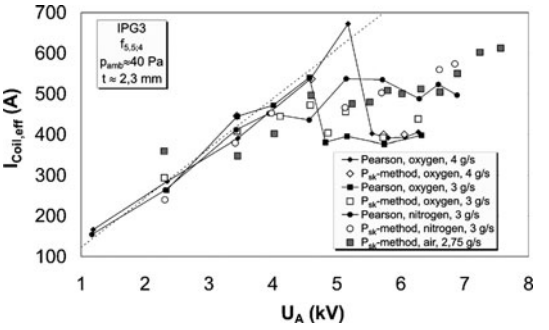


Figure 29. IPG3 ($t \approx 2.3$ mm) Pearson coil currents with estimated, corrected coil currents.

Then the current does not change anymore although the anode voltage is increased further. With the applied Bessel model one obtains a maximum magnetic pressure of about 275 Pa and a Lorentz force of approximately 4.5 N [37]. Here, a plasma radius of $R = 0.03$ m with a geometric assumption for the thermal boundary layer at the tube wall was assumed.

Similar behavior can be observed for 4 g s^{-1}. Here, the current increases almost linearly with the anode voltage. After 0.67 kA are reached, the current decreases to 0.4 kA and then remains constant with a further increase of U_A. With nitrogen similar behavior can be seen. However, the current does not behave as drastically as with oxygen. Currents of about 0.5–0.54 kA occur for $U_A > 5$ kV after the current history has left the common curve that has a slope of 0.122 A V^{-1}. The common curve for the low anode voltages may be explained by the low secondary effects of the low-power plasmas. With the second transition almost constant currents occur although the voltages are increased further.

According to (10), the measurement periods for the current monitor are limited. Hence, conditions where parameters such as, e.g., ambient pressure must be adjusted cannot be measured as the period to reach steady-state conditions is too long. The resonant circuit has an AC resistance consisting of coil inductivity, capacity of the used capacitors and the Ohmic resistances of the power lines. Ohmic losses, however, are signified by the Ohmic resistances. By calculating the resistance for the coil, the resonant circuit cooling power can be rebuilt based on the coil current. Then the effective coil current can be estimated:

$$I_{\mathrm{Coil,eff}} = \sqrt{\frac{K P_{\mathrm{SK}}}{R_{\mathrm{Coil,AC}}}}. \tag{53}$$

Here, K is about 3.6, the corresponding results are shown in Fig. 29 (P_{SK} method) and are in quite good agreement (maximum deviation 15%) with the results of the current monitor measurements. In Fig. 30 the measurements are related to electric field measurements.

An almost linear relationship can be observed resulting in a powerful tool to measure the coil currents indirectly using the EMR-200.

To analyze the operational conditions in the inductively heated plasma generator, the section of the IPG can be divided into three different zones in radial direction: the first zone is represented by the hot ring, in which the majority of the plasma power is assumed to be coupled in. Within this ring a center zone is located where σ

https://doi.org/10.1017/S0022377807006927 Published online by Cambridge University Press

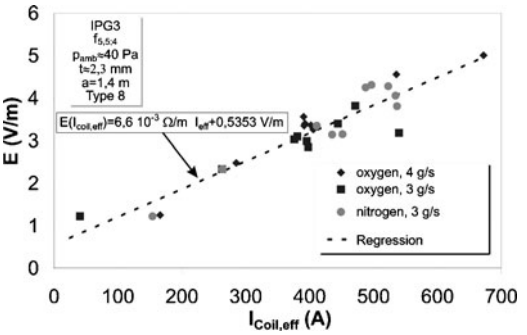


Figure 30. Electric field depending on $I_{\mathrm{coil,eff}}$, measured with EMR-200 at axial distance of 1.4 m.

is assumed to be zero. Between the inner wall of the tube and the hot ring a further zone can be distinguished representing the thermal boundary layer.

Using the calculated inner tube wall temperatures (see Fig. 26), the thickness of the thermal boundary layer using $\delta_{\mathrm{T}} = L/Nu$ can be estimated. Here, δ_{T} values of about 20 mm are obtained which has been confirmed by radial intensity and spectroscopic measurements in previous investigations [3, 5]. Furthermore, it is assumed that $\rho \cdot v$ is constant within the entire cross section of the tube. It has to be mentioned that this assumption is of a rather raw nature in the case that strong Lorentz forces occur during the operation of the IPG. In addition, $\sigma \approx 0$ is estimated for the thermal boundary layer. A similar method has been described by Raizer [38]. Consequently, the power coupling is restricted to a ring zone which is between the center zone ($\sigma \approx 0$) and the thermal boundary layer ($\sigma \approx 0$) at the tube's inner wall:

$$\frac{h_\delta}{h_{\mathrm{tot,eff}}} = \frac{A_{\mathrm{tot}}}{A_\delta} = \left(\frac{d}{d-2\delta_{\mathrm{T}}}\right)^2 \left[4\frac{\delta}{d-2\delta_{\mathrm{T}}}\left(1-\frac{\delta}{d-2\delta_{\mathrm{T}}}\right)\right]^{-1}. \tag{54}$$

With an inductive coupling $0 \leqslant \delta \leqslant R_{\mathrm{in}} - \delta_{\mathrm{T}}$ can be assumed, so that (54) has $h_{\delta,\mathrm{min}}/h_{\mathrm{tot,eff}} = (d/(d-2\cdot\delta_{\mathrm{T}}))^2$ as a minimum value. With (24) and (52) a boundary value problem (BVP) can be positioned:

$$p_{\mathrm{in}}, \delta, \delta_{\mathrm{T}} \xrightarrow{(39)} \frac{h_\delta}{h_{\mathrm{tot,eff}}} \xrightarrow{(35)} T_\delta \xrightarrow{(37)} \sigma_\delta \xrightarrow{(22)} \delta_{\mathrm{calc}}. \tag{55}$$

Here, the value δ is varied until $\delta = \delta_{\mathrm{calc}}$. In Fig. 31 the results for the conditions in Fig. 28 are shown. With the exception of $f_{5,5;4}$ the dependence of δ on the frequency (24) can be seen. The BVP cannot be solved for the most conditions if $P_{\mathrm{cal}} < 20$ kW. This can be explained as follows: for small powers the secondary effects and, hence, the damping is low such that the division of the tube's section into discrete zones is no longer valid. For large δ the assumption that the majority of the power is coupled into the zone which has a thickness of δ can no longer be maintained. A further result is that the curves for $f_{5.5;5}$ and $f_{5.5;6}$ intersect with the horizontal $(d - 2 \cdot \delta_{\mathrm{T}})/\delta = 3.6$, the position of the power maximum (32).

Considering Figs 16 and 28 the following conclusion can be made: for $n = 2.5$ the conditions are on the right-hand side of the maximum in Fig. 16, $(d-2\cdot\delta_{\mathrm{T}})/\delta > 3.6$. However, the total powers are higher than for $n = 5.5$ as confirmed by Figs 16 and 28. With increasing P_{cal} the histories for δ seem to get a reduced gradient. For

https://doi.org/10.1017/S0022377807006927 Published online by Cambridge University Press

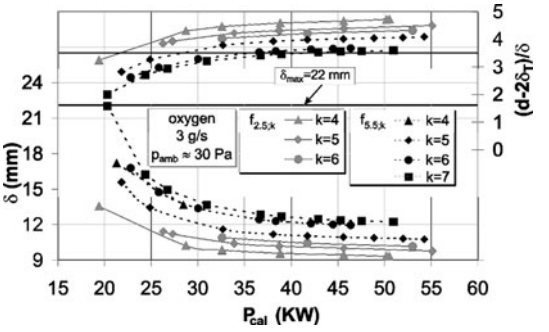


Figure 31. d and $(d - 2 \cdot \delta_T)/\delta$ for $\delta_T = 20$ mm depending on measured calorimetric power.

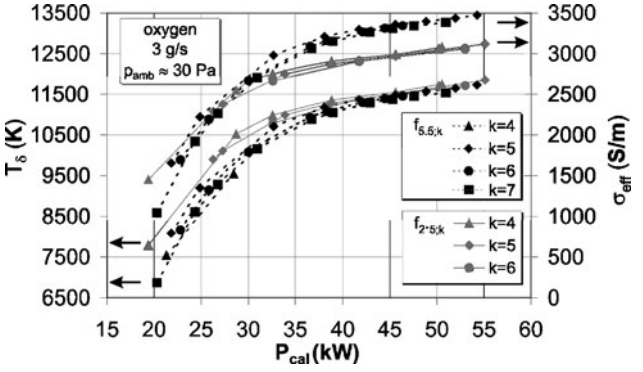


Figure 32. Temperatures and electric conductivities in plasma ring of thickness δ.

$n = 2.5$ the skin depth δ seems to have a lower limit of about 9–10.5 mm. For $n = 5.5$ the skin depth δ has values between 11 and 12 mm (depending on f).

By comparing the two curves for T_δ in Fig. 32, it can be seen that they are almost equal for high powers. In [5] numerical simulations for $f_{5.5;4}$ with $I_{\mathrm{coil,eff}} = 0.4$ kA ($P_{\mathrm{cal}} = 28$ kW) are presented. The results for T_e are slightly higher but correspond fairly well with $T_\delta = 9500$ K in Fig. 32. The same holds for ψ_e.

For σ_{eff} in Fig. 32 the behavior is just the opposite: the σ_{eff} curves are close together. They separate with increasing power. At the high plasma powers for $n = 2.5$ a maximum σ_{eff} of approximately 3100 S m^{-1} can be seen. For $n = 5.5$, $\sigma_{\mathrm{max,eff}} \approx 3500$ S m^{-1}. In Fig. 31 $\delta_{n=2.5}$ is lower than $\delta_{n=5.5}$. Taking into account the dependency shown in Fig. 32 this can be considered to be a frequency effect (24). The pressures in the tube belonging to the data in Fig. 32 are slightly higher for $n = 5.5$ and $P_{\mathrm{cal}} > 30$ kW than for $n = 2.5$, which confirms the behavior of σ_{eff} at these temperatures, see also Fig. 21. The low σ_{eff} can be explained by the geometry of the 2.5-turn coil: here, the distance between the coil turns is larger which may lead to a 'cooling' of the plasma in between the coil turns.

Considering Fig. 33 the following statements can be made: the curves for $f_{5,5;6}$ and $f_{5,5;7}$ have maxima that are in the same power region as the $(d - 2\delta_T)/\delta = 3.6$ values in Fig. 32. It has to be pointed out that such features may also be due to the overall behavior of the facility (e.g. triode). However, the following features are obvious.

https://doi.org/10.1017/S0022377807006927 Published online by Cambridge University Press

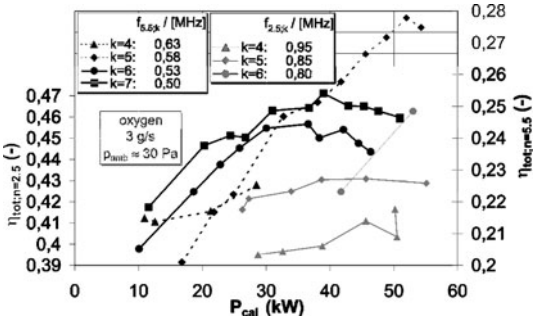


Figure 33. η_{tot} for oxygen plasmas over P_{cal} for different frequencies.

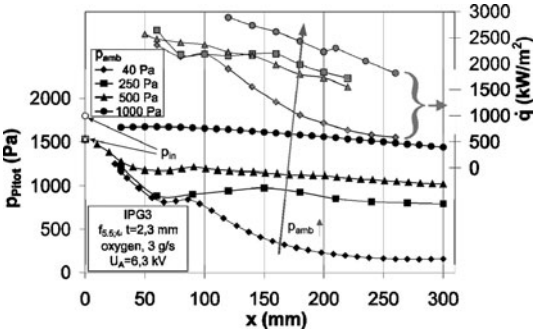


Figure 34. Pitot pressure (dark symbols) and heat flux profiles, transition from supersonic to sub-sonic flow with increasing tank pressure.

(a) The reduction of n from 5.5 to 2.5 leads to an increase in efficiency. The analysis of (34) shows that P_{Pl} is proportional to $f^{0,5}$ provided that the coil current does not change.

(b) The maxima for h_{tot} are between 35 and 50 kW. Here, the optimal positions for $(d - 2 \cdot \delta_{\mathrm{T}})/\delta$ are found as well (= 3.6). They can be explained using (34).

6.2. Characterization of the plasma flow

The flow conditions in the PWK were investigated using different measurement techniques. Here, the reference conditions were chosen in correspondence with the investigations made in the previous section. The reference conditions are summarized as follows: $U_A = 6.3$ kV, $P_A = 110$ kW, $I_{\mathrm{coil,eff}} = 395$ A, mass flow rate 3 g s^{-1}, $p_{\mathrm{amb,min}} = 40$ Pa, $P_{\mathrm{cal}} = 28$ kW, $f_{5.5;4}$, silicon carbide material sample temperatures $T_{\mathrm{SiC}}(x \geqslant 90\ \mathrm{mm}) \leqslant 2125$ K.

Figures 34 and 35 depict the corresponding heat flux and Pitot pressure profiles in PWK3. Figure 34 shows the profiles for ambient pressures of 40 Pa, 2.5 hPa, 5 hPa and 10 hPa. The curves with the symbols filled in grey refer to the heat fluxes and are related to the right axis. Generally, the low-pressure curves have axial pressure profiles with both inflection and extremal points. This is typical for supersonic flow conditions and has already been observed quite often for other supersonic plasma facilities [30]. Similar behavior can be observed for the heat flux profiles. It can be seen that both Pitot pressure and heat flux curves increase with increasing ambient pressure. For the first three conditions $p_{\mathrm{Pitot}}/p_{\mathrm{amb}}$ is larger than 2. Such values are

https://doi.org/10.1017/S0022377807006927 Published online by Cambridge University Press

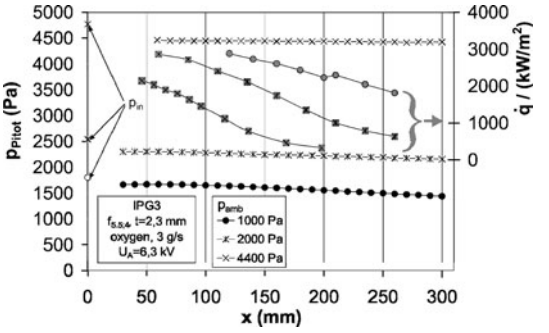


Figure 35. Pitot pressure and heat flux profiles, variation of tank pressure (subsonic).

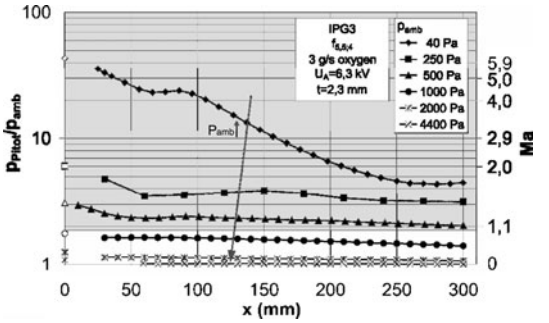


Figure 36. Axial profiles of $p_{\mathrm{Pitot}}/p_{\mathrm{amb}}$ and Mach number, variation of tank pressure.

representative for supersonic flow conditions. At $x = 0$ the measured inner tube pressures are shown with the white symbols. One can observe that these pressures do not change with the increasing ambient pressure up to 5 hPa. This confirms that for these conditions no communication between the PWK and IPG is present. With $p_{\mathrm{amb}} = 10$ hPa the fraction $p_{\mathrm{Pitot}}/p_{\mathrm{amb}}$ is smaller than 2 for all x which leads to the statement that this condition is subsonic. This can also be confirmed by p_{in} (18 hPa) as this pressure has now increased with the increased tank pressure. Therefore, the inductively heated facility PWK3 is, in contrast to the statements of Bottin [22], capable of generating both supersonic and subsonic flow conditions.

In Fig. 35 similar observations are made for the measured Pitot pressure profiles. The ambient pressure in PWK3 is increased further leading to a further increase of the pressure in the tube. The transition between supersonic and subsonic flow conditions occurs between 5 and 10 hPa. In general, the pressure in the tube allows for the statement concerning the upper limit of the Pitot pressure in the PWK. However, the behavior of the heat fluxes has changed. At these pressure levels they decrease with increasing ambient pressure. The maximum heat flux profile is obtained for $p_{\mathrm{amb}} = 10$ hPa.

Figure 36 depicts $p_{\mathrm{Pitot}}/p_{\mathrm{amb}}$ for all conditions from Figs 34 and 35. The right axis shows the Mach numbers based on the regression curve shown in Fig. 10. The grey zone highlights the supersonic regime, the white zone indicates the subsonic region. The ratio $p_{\mathrm{Pitot}}/p_{\mathrm{amb}}$ and the Mach numbers and flow velocities decrease with increasing p_{amb}. The wedge probe can only be used for $p_{\mathrm{amb}} \approx 40$ Pa owing to the shock detachment according to Eq. (17). Figure 37 depicts the Mach number profiles based on the Rayleigh–Pitot formula (13) together with wedge probe

https://doi.org/10.1017/S0022377807006927 Published online by Cambridge University Press

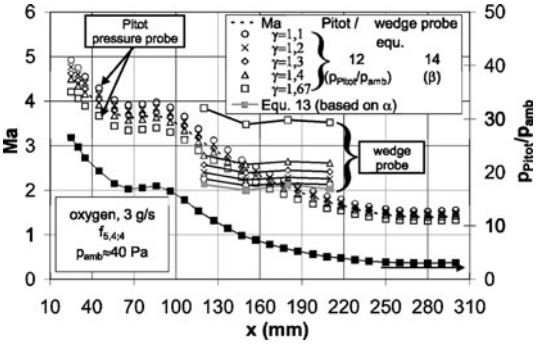


Figure 37. Comparison of Mach number profiles using Pitot and wedge probe measurement.

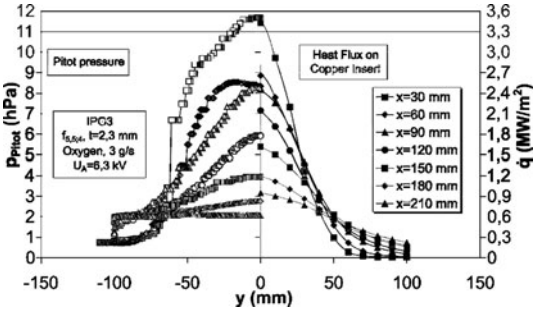


Figure 38. Radial profiles for Pitot pressure and heat flux; variation of axial distance.

measurements. For the lower γ a good agreement between both measurements can be seen. Mach numbers for $x \geqslant 150$ mm correspond fairly well. For $x = 120$ mm the correspondence is worse for higher γ. Comparing the Mach numbers from (15) and (16) the correspondence is quite good for γ close to 1.

This is consistent with the results from the Rayleigh–Pitot formula which leads to the presumption that γ is actually close to 1. Equations (15) and (16) deliver values between 1 and 1.08. The significance of these values is evident: the heat capacities c_p and c_v are close to each other owing to excitation and chemical reactions. The significance of this is not that drastic. However, γ values in the interval $[1.1; 1.2]$ deliver rather good results if simple one-dimensional shock equations are used [22]. The curve for $\gamma = 1.67$ shows that this value is rather implausible which confirms statements in [22].

Using the mean enthalpy (9) the local specific enthalpies can be estimated based on the radial profiles for Pitot pressure and heat flux as shown in Fig. 38. Here, the following relationship was used assuming that the mean enthalpy determined with the calorimeter is distributed radially [5]:

$$\frac{h_{\mathrm{tot,e}}(x,y)}{h_{\mathrm{Kal,eff}}} \approx \frac{R_{\mathrm{Pl}}^2}{2} \frac{(\dot{q}/\sqrt{p_{\mathrm{tot}}})(x,y)}{\int_0^{R_{\mathrm{Pl}}} (\dot{q}/\sqrt{p_{\mathrm{tot}}}) y \, dy}. \tag{56}$$

The numerical results in [5] for $I_{\mathrm{coil}} = 400$ A show that oxygen at the IPG outlet is fully dissociated, a good correspondence with the results obtained from equilibrium considerations shown in Fig. 39. The corresponding local specific enthalpies were

https://doi.org/10.1017/S0022377807006927 Published online by Cambridge University Press

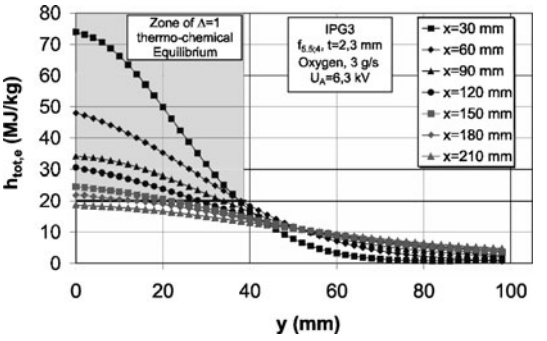


Figure 39. Radial profiles of the local specific enthalpies.

Table 1. Summary of plasma condition at $x = 130$ mm.

Parameter	Value	Remark	Reference
$\dot{q}$ (MW m^{-2})	1.7		[5]
p_{Pitot} (Pa)	530		[5]
p_{Ambient} (Pa)	40	Tank pressure	See also [5]
Ma	2.8	Wedge/Pitot pressure probe	See Fig. 37
h (MJ kg^{-1})	$<30.5/33.7 \pm 2.9$	30.5, see also Fig. 39	[5]/[29]
T_{trans} (K)	9500	Maximum value (time dependent)	[29]
Δ	1/0.92	Enthalpy model/ measured T and densities	[5]/[29]
γ	1–1.1	Wedge probe	See also [5]
a (km s^{-1})	2	Estimated from T in [29] and γ	
v (km s^{-1})	5.6/5.6	6.4 estimated with a and Ma	—/[29]

cross-checked with data from other independent measurement technologies such as laser diode absorption spectroscopy [29] and laser-induced fluorescence [39]. The results that were obtained for the reference condition with $p_{\text{amb}} = 40$ Pa at the position $x = 130$ mm in the center of the plasma jet correspond within 10% of each other.

In Table 1 the overall parameter that were determined for this condition are shown as a summary.

Axial profiles of the dissociation degree were also determined in [40] and [41] where a new probe technology was applied. Here, two different material inserts were used simultaneously. The differences in heat flux owing to the different but known emissivities and recombination histories were evaluated. Using an approbate boundary layer model, the dissociation degree could be determined.

7. Summary

Within the scope of this work the inductively driven plasma wind tunnel PWK3 to investigate heat shield materials for space vehicles entering a celestial body's atmosphere has been described. Besides the construction and assembly of the facility, the inductively heated plasma generators IPG3, IPG4 and IPG5 have been outlined. These plasma generators were commissioned together with the plasma

https://doi.org/10.1017/S0022377807006927 Published online by Cambridge University Press

wind tunnel facility and qualified for both the simulation of atmospheric entry manoeuvres and basic tests in the field of material catalysis and oxidation behavior. In addition to the computer-assisted measurement techniques for the performance and monitoring of the experiments, a set of measurement techniques has been applied. In particular, there are the cavity calorimeter for the measurement of the thermal plasma power, the system EMR-200 to measure electric and magnetic fields and the Pearson current measurement system which was adapted and qualified for PWK3. The Pearson current monitor has been modified with the support of the Institut für Leistungselektronik of the Universität Stuttgart and Pearson Inc. The newly developed HOKA sensor was successfully operated. The quasi-stationary mode of operation enabled time-consuming measurements at high power and frequency. The applied measurement techniques have been used to characterize both plasma generator and plasma flow condition in the plasma wind tunnel. For the latter, probe techniques have been used such as heat flux probes, material probes, wedge probes and Pitot pressure probes.

A family of inductively driven plasma generators IPG3, IPG4 and IPG5 has been developed in order to cope with the different demands of diverse applications. The understanding of both the functional behavior of the facility and the plasma generators could be significantly improved owing to the results of the performed measurements. The measured electrodynamic data as well as the power balances, which result from the measurement of plasma power and cooling powers, expand into the numerical simulation of plasma generator and facility. Here, parameters such as the number of capacitors of the resonant circuit, inductivity of the primary coil, wall thickness of the plasma tube as well as gas composition, gas mass flow rate and ambient pressure have been varied in order to perform an optimization. In this manner, a maximization of efficiency and plasma power could be achieved for steady-state high-enthalpy conditions using oxygen as working gas.

The operational characteristics of the inductively driven plasma generators could be rebuilt using one-dimensional models based on averaged parameters. These models have also been applied as a lay-out design tool for the development of other plasma generators such as IPG5. Here, the frequency dependency of the induced plasma power, the optimization of the efficiency, the maximization of the power coupling as well as the explanation of observed and measured operational states using MHD processes are to be mentioned as examples. Both magnetic pressure and Lorentz force are of a magnitude that allows the statement that fundamental understanding of IPG's operational behavior requires consideration of MHD effects. As an example, the tube cooling phenomenon regarding the second transition accompanied by the supersonic flow can be explained by these MHD effects. Estimations concerning the Stewart and magnetic Reynolds number approve this argumentation.

The developed and applied models could be compiled using the Maxwell equations. Together with thermodynamic equilibrium models for plasma composition, density, electrical conductivity as well as specific enthalpy these models represent the basis for the functional description of inductively heated plasma generators. The connection between electrodynamic and thermodynamic models resulted from an initial value problem by using the calorimetrically measured mean enthapies in order to determine the equilibrium temperature with the enthalpy model. This temperature is then used for the calculation of the electrical conductivity. Before this, a validation of the calculated electrical conductivities was performed using literature data. Having determined the electrical conductivity, the

https://doi.org/10.1017/S0022377807006927 Published online by Cambridge University Press

skin depth was calculated, which is a very important parameter for understanding the facility.

Concerning the flow conditions, the facility enables both subsonic and supersonic conditions, which is a quite particular feature as most of the existing inductively driven plasma wind tunnels can mostly cope with sub-sonic conditions only. The required conditions, e.g. the high plasma powers as well as the heat fluxes in order to realize the active oxidation of silicon carbide based heat shield materials and the simulation of atmospheric entries at Mars and Venus, could be put into operation. The investigation of the flow concerning its composition (dissociation degree) together with the possibility of operating the facility with single gases, such as oxygen, represent a basis for further investigations of the reaction mechanisms in front of a heat shield material sample.

Acknowledgement

The authors thank all members of the group who helped to perform the described measurement campaigns.

Appendix A. Help functions

In order to simplify the evaluation of the solutions given by (25)–(27), the complex Bessel functions J_0, J_0^2, J_1 and some of their derivatives were separated into real and imaginary parts according to

$$A\left(\frac{\delta}{R}\right) = \frac{1}{R}\mathrm{Re}\left[\int_0^R J_0^2\left(\sqrt{-2i}\frac{r}{\delta}\right) dr\right], \tag{A 1}$$

$$B\left(\frac{\delta}{R}\right) = \frac{1}{R}\mathrm{Im}\left[\int_0^R J_0^2\left(\sqrt{-2i}\frac{r}{\delta}\right) dr\right], \tag{A 2}$$

$$C\left(\frac{\delta}{R}\right) = \mathrm{Re}\left[J_0^2\left(\sqrt{-2i}\frac{R}{\delta}\right)\right], \tag{A 3}$$

$$D\left(\frac{\delta}{R}\right) = \mathrm{Im}\left[J_0^2\left(\sqrt{-2i}\frac{R}{\delta}\right)\right], \tag{A 4}$$

$$F\left(\frac{\delta}{R}\right) = \mathrm{Re}\left[J_0\left(\sqrt{-2i}\frac{R}{\delta}\right)\right], \tag{A 5}$$

$$G\left(\frac{\delta}{R}\right) = \mathrm{Im}\left[J_0\left(\sqrt{-2i}\frac{R}{\delta}\right)\right], \tag{A 6}$$

$$K\left(\frac{\delta}{R}\right) = \mathrm{Re}\left[J_1\left(\sqrt{-2i}\frac{R}{\delta}\right)\right] \tag{A 7}$$

and

$$L\left(\frac{\delta}{R}\right) = \mathrm{Im}\left[J_1\left(\sqrt{-2i}\frac{R}{\delta}\right)\right]. \tag{A 8}$$

Depending on the literature, the functions F and G are known as Kelvin or Thomson functions. A first kind Bessel function is defined by

$$J_n(z) = \sum_{m=0}^{\infty} \frac{(-1)^m}{m!(n+m)!}\left(\frac{z}{2}\right)^{n+2m}, \tag{A 9}$$

https://doi.org/10.1017/S0022377807006927 Published online by Cambridge University Press

where the argument z is complex and the order n is zero or positive integer [42]. This leads to

$$J_0(z) = \sum_{m=0}^{\infty} \frac{(-1)^m}{(m!)^2} \left(\frac{z}{2}\right)^{2m} \tag{A 10}$$

and

$$J_1(z) = \sum_{m=0}^{\infty} \frac{(-1)^m}{m!(1+m)!} \left(\frac{z}{2}\right)^{1+2m}. \tag{A 11}$$

The general equation for squared Bessel functions is

$$J_n^2(z) = \sum_{m=0}^{\infty} \frac{(-1)^m (2n+2m)!}{m!(2n+m)![(n+m)!]^2} \left(\frac{z}{2}\right)^{2n+2m}. \tag{A 12}$$

Accordingly, one obtains

$$J_0^2(z) = \sum_{m=0}^{\infty} \frac{(-1)^m (2m)!}{(m!)^4} \left(\frac{z}{2}\right)^{2m}. \tag{A 13}$$

Knowing that $z = aR$ with $a = (1-i)/\delta$, one can see that the central term responsible for receiving an overall complex result can be reduced to $(1-i)^{2m}$. Sampling the control variable m shows that all even numbers of m yield real and all odd numbers of m result in imaginary terms. Consequently, one can write $(-1)^m 2^{2m}$ in the first case and $(-1)^m 2^{2m-1}$ in the latter. Applying these results to (A 9) and (A 12) yields

$$A\left(\frac{\delta}{R}\right) = \sum_{m=0}^{\infty} \frac{(-1)^m (4m)!}{2^{2m}(4m+1)[(2m)!]^4} \left(\frac{R}{\delta}\right)^{4m}, \tag{A 14}$$

$$B\left(\frac{\delta}{R}\right) = -\sum_{m=1}^{\infty} \frac{(-1)^m (4m-2)! 2^{2m}}{2(4m-1)[(2m-1)!]^4} \left(\frac{R}{2\delta}\right)^{4m-2}, \tag{A 15}$$

$$C\left(\frac{\delta}{R}\right) = \sum_{m=0}^{\infty} \frac{(-1)^m (4m)!}{2^{2m}[(2m)!]^4} \left(\frac{R}{\delta}\right)^{4m}, \tag{A 16}$$

$$D\left(\frac{\delta}{R}\right) = -\sum_{m=1}^{\infty} \frac{(-1)^m (4m-2)! 2^{2m}}{2[(2m-1)!]^4} \left(\frac{R}{2\delta}\right)^{4m-2}, \tag{A 17}$$

$$F\left(\frac{\delta}{R}\right) = \sum_{0}^{\infty} \frac{(-1)^m}{2^{2m}[(2m)!]^2} \left(\frac{R}{\delta}\right)^{4m}, \tag{A 18}$$

$$G\left(\frac{\delta}{R}\right) = -\sum_{1}^{\infty} \frac{(-1)^m 2^{2m}}{2[(2m-1)!]^2} \left(\frac{R}{2\delta}\right)^{4m-2}, \tag{A 19}$$

$$K\left(\frac{\delta}{R}\right) = K_1\left(\frac{\delta}{R}\right) + K_2\left(\frac{\delta}{R}\right) \tag{A 20}$$

and

$$L\left(\frac{\delta}{R}\right) = -K_1\left(\frac{\delta}{R}\right) + K_2\left(\frac{\delta}{R}\right), \tag{A 21}$$

https://doi.org/10.1017/S0022377807006927 Published online by Cambridge University Press

with

$$K_1\left(\frac{\delta}{R}\right) = \sum_0^\infty \frac{(-1)^m 2^{2m}}{(2m+1)[(2m)!]^2}\left(\frac{R}{2\delta}\right)^{4m+1} \tag{A 22}$$

and

$$K_2\left(\frac{\delta}{R}\right) = -\sum_1^\infty \frac{(-1)^m 2^{2m}}{4m[(2m-1)!]^2}\left(\frac{R}{2\delta}\right)^{4m-1}. \tag{A 23}$$

Obviously, the attenuation factor δ/R is the independent variable. Radial dependency can be expressed by replacing R by r. The unknown attenuation δ follows then from different δ/R relations for known (and fix) R.

References

[1] Hittorf, W. 1884 Ueber die Electricitaetsleitung der Gase. *Ann. Phys. Chem.* **21**, 90–139.

[2] McKinnan, K. A. 1929 On the origin of the electrodeless discharge. *Philos. Mag. J. Sci., Ser. 7* **8**(52), 601–616.

[3] Herdrich, G., Auweter–Kurtz, M. and Kurtz, H. 2000 New inductively heated plasma source for reentry simulations. *J. Thermophys. Heat Transfer* **14**(2), 244–249.

[4] Thomson, J. J. 1891 On the discharge of electricity through exhausted tubes without electrodes. *Philos. Mag. J. Sci., Ser. 5* **32**(197), 321–464.

[5] Herdrich, G. 2004 Aufbau, Qualifikation und Charakterisierung einer induktiv beheizten Plasmawindkanalanlage zur Simulation atmosphärischer Eintrittsmanöver. Dissertation, Institut für Raumfahrtsysteme, Universität Stuttgart, December.

[6] Eckert, H. U. 1984 The hundred year history of induction discharges. *Proc. 2nd Annual Int. Conf. of Chemistry and Technology* (ed. H. V. Boenig).

[7] Thomson, J. J. 1927 The electrodeless discharge through gases. *Philos. Mag. J. Sci., Ser. 7* **4**(25), 1128–1160.

[8] Freeman, M. P. and Chase, J. D. 1968 Energy-transfer mechanism and typical operating characteristics for the thermal rf plasma generator. *J. Appl. Phys.* **39**(1), 180–190.

[9] Eckert, H. U. 1962 Diffusion theory of the electrodeless ring discharge. *J. Appl. Phys.* **33**(9), 2780–2788.

[10] Henrikson, B. B., Keefer, D. R. and Clarkson, M. H. 1971 Electromagnetic field in electrodeless discharge. *J. Appl. Phys.* **42**(13), 5460–5464.

[11] Herdrich, G., Auweter-Kurtz, M., Kurtz, H. L., Laux, T. and Winter, M. 2002 Operational behavior of the inductively heated plasma source IPG3 for re-entry simulations. *J. Thermophys. Heat Transfer* **16**(3), 440–449.

[12] Boulos, M. I., Gagne, R. and Barnes, R. 1980 Effect of Swirl and confinement on the flow and temperature fields in an inductively coupled r.f. plasma. *Can. J. Chem. Eng.* **58**, 367–375.

[13] Miller, R. C. and Ayen, R. J. 1969 Temperature profiles and energy balances for an inductively coupled plasma torch. *J. Appl. Phys.* **40**(13), 5260–5273.

[14] Eckert, H. U. 1970 Analysis of thermal plasmas dominated by radial conduction losses. *J. Appl. Phys.* **41**(4), 1520–1528.

[15] Pridmore-Brown, D. C. 1970 Numerical study of the inductive electrodeless discharge. *J. Appl. Phys.* **41**(9), 3621–3625.

[16] Barnes, R. M. and Nikdel, S. 1976 Temperature and velocity profiles and energy balances for inductively coupled plasma discharge in nitrogen. *J. Appl. Phys.* **47**(9), 3929–3934.

[17] Mostaghimi, J., Proulx, P. and Boulos, M. I. 1984 Parametric study of the flow and temperature fields in an inductively coupled r.f. plasma torch. *Plasma Chem. Plasma Process.*, **4**(3), 199–217.

https://doi.org/10.1017/S0022377807006927 Published online by Cambridge University Press

[18] McKelliget, J. W. and El-Kaddah, N. 1988 The effect of coil design on material synthesis in an inductively heated plasma torch. *J. Appl. Phys.* **64**(6), 2948–2958.

[19] Yang, P., Barnes R. M., Mostaghimi, J. and Boulos, M. I. 1989 Application of a two-dimensional model in the simulation of an analytical inductively coupled plasma discharge. *Spectrochimica Acta*, **44B**(7), 657–666.

[20] Gordeev, A. N. 1999 Overview of characteristics and experiments in IPM plasmatrons. *RTO AVT/VKI Special Course on Measurement Techniques for High Enthalpy Plasma Flows*, RTO EN-1, von Karman Institute for Fluid Dynamics, Rhode-Saint-Genèse, Belgium, October.

[21] Kolesnikov, A. F. 1999 Combined measurements and computations of high enthalpy and plasma flows for determination of TPM surface catalycity. *RTO AVT/VKI Special Course on Measurement Techniques for High Enthalpy Plasma Flows*, RTO EN-1, von Karman Institute for Fluid Dynamics, Rhode-Saint-Genèse, Belgium, October.

[22] Bottin, B. 1999 Aerothermodynamic model of an inductively-coupled plasma wind tunnel. Thesis for Docteur en Sciences Appliquées, Université de Liège, Faculté des Sciences Appliquées, von Karman Institute for Fluid Dynamics, Aeronautics/Aerospace Department.

[23] Lenzner, S., Auweter-Kurtz, M., Heiermann, J. and Sleziona, P. C. 2000 Energy partitions in inductively heated plasma sources for re-entry simulations. *J. Thermophys. Heat Transfer* **14**(3), 388–395.

[24] Mekidéche, M. R. 1993 Contribution à la modélisation numérique de torches de plasma d'induction. Thèse de doctorat, Ecole doctorale sciences pour l'ingénieur de Nantes, October.

[25] Herdrich, G., Auweter-Kurtz, M. and Endlich, P. 2003 Mars entry simulation using the inductively heated plasma generator IPG4. *J. Spacecraft Rockets* **40**(5), 690–694.

[26] Auweter-Kurtz, M. and Wegmann, Th. 1999 Overview of IRS plasma wind tunnel facilities. *RTO AVT/VKI Special Course on Measurement Techniques for High Enthalpy Plasma Flows*, RTO EN-8, von Karman Institute for Fluid Dynamics, Rhode-Saint-Genèse, Belgium, October.

[27] Pidan, S., Auweter-Kurtz, M., Herdrich, G. and Fertig, M. 2005 Recombination coefficients and spectral emissivity of silicon carbide-based thermal protection materials. Paper AIAA 2004-2274, 37th AIAA Thermophysics Conference, Portland, Oregon, USA, June/July 2004. *J. Thermophys. Heat Transfer* **19**(4), 566–571.

[28] Herdrich, G., Auweter-Kurtz, M., Fertig, M., Löhle, S., Pidan, S. and Laux, T. 2005 Oxidation behaviour of SiC-based thermal protection system materials using newly developed probe techniques. Paper AIAA 2004-2173, 37th AIAA Thermophysics Conference, Portland, Oregon, USA, June/July 2004. *J. Spacecraft Rockets* **42**(5), 817–824.

[29] Matsui, M.[1], Komurasaki, K.[4], Herdrich, G.[2] and Auweter-Kurtz, M.[3] 2005 Enthalpy measurement in inductive plasma generator flow by laser absorption spectroscopy. [1,4]Department of Advanced Energy, The University of Tokyo, Kashiwanoha 5-1-5, Kashiwa, Chiba 277-8562, Japan, [2,3]Institut für Raumfahrtsysteme, Universität Stuttgart. *AIAA Journal* **43**(9), 2060–2064.

[30] Auweter-Kurtz, M., Feigl, M. and Winter, M. 1999 Diagnostic tools for plasma wind tunnels and re-entry vehicles at the IRS. *RTO AVT/VKI Special Course on Measurement Techniques for High Enthalpy Plasma Flows*, RTO EN-8, von Karman Institute for Fluid Dynamics, Rhode-Saint-Genèse, Belgium, October.

[31] Auweter-Kurtz, M., Fertig, M., Herdrich, G., Laux, T., Schöttle, U., Wegmann, Th., Winter M. 2003 Entry experiments at IRS – in-flight measurement during atmospheric entries. 53rd Int. Astronautical Congress, Houston, TX, USA, October 2002. *Space Technol. Journal* **23**(4) 217–234.

[32] Herdrich, G. and Auweter-Kurtz, M. 2006 Inductively heated plasma sources for technical applications. *Vacuum J.* **80**, 1138–1143.

[33] Karrer, N., Hofer-Noser, P., Herdrich, G. and Auweter-Kurtz, M. 2003 Isolated current probe for continuous monitoring of AC currents of high amplitude and high frequency.

https://doi.org/10.1017/S0022377807006927 Published online by Cambridge University Press

10th European Conference on Power Electronics and Applications, Toulouse, France, 2–4 September.

[34] Simpson, P. G. 1960 *Induction Heating—Coil and System Design*. New York: McGraw-Hill.

[35] Sleziona, P. C. 1992 Numerische Analyse der Strömungsvorgänge in magnetoplasmadynamischen Raumfahrtantrieben. Dissertation, Institut für Raumfahrtsysteme, Universität Stuttgart.

[36] Bykova, N. G., Vasil'evskii, S. A., Gordeev, A. N., Kolesnikov, A. F., Pershin, I. S. and Yakushin, M. I. 1997 Determination of the effective probabilities of catalytic reactions on the surfaces of heat shield materials in dissociated carbon dioxide flows. *J. Fluid Dynam.* **32**(6), 876–886.

[37] Herdrich, G., Auweter-Kurtz, M., Fertig, M., Nawaz, A. and Petkow, D. 2006 MHD flow control for plasma technology applications. *Vacuum J.* **80**, 1167–1173.

[38] Raizer, Y. P. 1991 *Gas Discharge Physics*. Berlin: Springer.

[39] Löhle, S. 2006 *Untersuchung von Wiedereintrittsplasmen mit Hilfe laserinduzierten Fluoreszenzmessungen*. Göttingen: Sierke.

[40] Pidan, S., Auweter-Kurtz, M., Herdrich, G. and Fertig, M. 2005 Recombination coefficients and spectral emissivity of silicon carbide-based thermal protection materials. Paper AIAA 2004-2274, 37th AIAA Thermophysics Conference, Portland, Oregon, USA, June/July 2004. *J. Thermophys. Heat Transfer* **19**(4), 566–571.

[41] Herdrich, G., Auweter-Kurtz, M., Fertig, M., Fischer, W., Muylaert, J.-M., Pidan, S., Schüßler, M. and Trabandt, U. 2006 Catalysis of TPS Materials for EXPERT TPS design and catalysis based in-flight instrumentations. *European Workshop on Thermal Protection Systems and Hot Structures*, May 2006, Noordwijk, The Netherlands, European Space Agency.

[42] Watson, G. N. 1958 *A Treatise on the Theory of Bessel Functions*, 2nd edn. Cambridge: Cambridge University Press.

https://doi.org/10.1017/S0022377807006927 Published online by Cambridge University Press